PSZ2LenS. Weak lensing analysis of the *Planck* clusters in the CFHTLenS and in the RCSLenS

Mauro Sereno,[1,2]⋆ Giovanni Covone,[3,4] Luca Izzo,[5] Stefano Ettori,[1,6] Jean Coupon[7] and Maggie Lieu[8]

[1]*INAF – Osservatorio Astronomico di Bologna, via Piero Gobetti 93/3, I-40129 Bologna, Italy*

[2]*Dipartimento di Fisica e Astronomia, Università di Bologna, via Piero Gobetti 93/2, I-40129 Bologna, Italy*

[3]*Dipartimento di Fisica, Università di Napoli 'Federico II', Compl. Univers. di Monte S. Angelo, via Cinthia, I-80126 Napoli, Italia*

[4]*INFN, Sezione di Napoli, Compl. Univers. di Monte S. Angelo, via Cinthia, I-80126 Napoli, Italia*

[5]*Instituto de Astrofísica de Andalucía (IAA-CSIC), Glorieta de la Astronomìa s/n, E-18008 Granada, Spain*

[6]*INFN, Sezione di Bologna, viale Berti Pichat 6/2, I-40127 Bologna, Italia*

[7]*Department of Astronomy, University of Geneva, ch. d'Ecogia 16, CH-1290 Versoix, Switzerland*

[8]*European Space Astronomy Centre (ESA/ESAC), Science Operations Department, E-28691 Villanueva de la Caada, Madrid, Spain*

ABSTRACT

The possibly unbiased selection process in surveys of the Sunyaev Zel'dovich effect can unveil new populations of galaxy clusters. We performed a weak lensing analysis of the PSZ2LenS sample, i.e. the PSZ2 galaxy clusters detected by the *Planck* mission in the sky portion covered by the lensing surveys CFHTLenS and RCSLenS. PSZ2LenS consists of 35 clusters and it is a statistically complete and homogeneous subsample of the PSZ2 catalogue. The *Planck* selected clusters appear to be unbiased tracers of the massive end of the cosmological haloes. The mass–concentration relation of the sample is in excellent agreement with predictions from the Λ cold dark matter model. The stacked lensing signal is detected at 14σ significance over the radial range $0.1 < R < 3.2\,\mathrm{Mpc}\,h^{-1}$, and is well described by the cuspy dark halo models predicted by numerical simulations. We confirmed that *Planck* estimated masses are biased low by $b_{SZ} = 27 \pm 11(\mathrm{stat}) \pm 8(\mathrm{sys})$ per cent with respect to weak lensing masses. The bias is higher for the cosmological subsample, $b_{SZ} = 40 \pm 14(\mathrm{stat}) \pm 8(\mathrm{sys})$ per cent.

Key words: gravitational lensing: weak – galaxies: clusters: general – galaxies: clusters: intracluster medium.

1 INTRODUCTION

The prominent role of clusters of galaxies in cosmology and astrophysics demands for a very accurate knowledge of their properties and history. Galaxy clusters are laboratories to study the physics of baryons and dark matter in the largest gravitationally nearly virialized regions (Voit 2005; Pratt et al. 2009; Arnaud et al. 2010; Giodini et al. 2013). Cosmological parameters can be determined with cluster abundances and the observed growth of massive haloes (Mantz et al. 2010; Planck Collaboration et al. 2016c), gas fractions (Ettori et al. 2009) or lensing analyses (Sereno 2002; Jullo et al. 2010; Lubini et al. 2014).

Ongoing and future large surveys will provide invaluable information on the multiwavelength sky (Laureijs et al. 2011; Pierre et al. 2016). Large surveys of the Sunyaev Zel'dovich (SZ) sky can find galaxy clusters up to high redshifts. Successful programs have been carried out by the *Planck* Satellite (Planck Collaboration

et al. 2016a), the South Pole Telescope (Bleem et al. 2015, SPT) and the Atacama Cosmology Telescope (Hasselfield et al. 2013, ACT). SZ surveys should in principle detect clusters regardless of their distance. Even though the finite spatial resolution can hamper the detection of the most distant objects, SZ selected clusters should be nearly mass limited. The selection function of SZ selected clusters can be well determined.

Furthermore, SZ quantities are quite stable and not significantly affected by dynamical state or mergers (Motl et al. 2005; Battaglia et al. 2012; Krause et al. 2012). The relation between mass and SZ flux is expected to have small intrinsic scatter (Battaglia et al. 2012; Kay et al. 2012). These properties make the determination of cosmological parameters using number counts of SZ detected clusters very appealing (Planck Collaboration et al. 2016a).

If confirmed, the mass limited but otherwise egalitarian selection could make the SZ clusters an unbiased sample of the whole massive haloes in the universe. Rossetti et al. (2016) characterized the dynamical state of 132 *Planck* clusters with high signal to noise ratio using as an indicator the projected offset between the peak of the X-ray emission and the position of the brightest cluster galaxy

(BCG). They showed that the fraction of dynamically relaxed objects is smaller than in X-ray selected samples and confirmed the early impression that many *Planck* selected objects are dynamically disturbed systems. Rossetti et al. (2017) found that the fraction of cool core clusters is 29 ± 4 per cent and does not show significant time evolution. They found that SZ selected samples are nearly unbiased towards cool cores, one of the main selection effects affecting clusters selected in X-ray surveys.

A crucial ingredient to study cluster physics is the mass determination. Weak lensing (WL) analyses can provide accurate and precise estimates. The physics behind gravitational lensing is very well understood (Bartelmann & Schneider 2001) and mass measurements can be provided up to high redshifts (Hoekstra et al. 2012; Umetsu et al. 2014; von der Linden et al. 2014a; Sereno 2015).

The main sources of uncertainty and scatter in WL mass estimates are due to triaxiality, substructures and projection effects (Oguri et al. 2005; Meneghetti et al. 2010; Becker & Kravtsov 2011; Sereno & Umetsu 2011; Bahé, McCarthy & King 2012; Giocoli et al. 2014). Theoretical predictions based on numerical simulations (Becker & Kravtsov 2011; Rasia et al. 2012) and recent measurements (Mantz et al. 2015; Sereno & Ettori 2015b) agree on an intrinsic scatter of ∼15 per cent.

More than 500 clusters with known WL mass are today available (Sereno 2015) and this number will explode with future large photometric surveys, e.g. Hyper Suprime-Cam Subaru Strategic Program (Aihara et al. 2017, HSC-SSP) or Euclid (Laureijs et al. 2011). However, direct mass measurements are usually available only for the most massive clusters. Mass estimates of lesser clusters have to rely on calibrated mass–observable relations (Sereno & Ettori 2017). Due to the low scatter, mass proxies based on SZ observables are among the most promising.

The above considerations motivate the analysis of SZ selected clusters of galaxies with homogeneous WL data. The relation between WL masses and SZ flux of *Planck* selected clusters has been investigated by several groups (Gruen et al. 2014; von der Linden et al. 2014b; Sereno, Ettori & Moscardini 2015; Smith et al. 2016). The scaling relation between WL mass and integrated spherical Compton parameter Y_{500} of the 115 *Planck* selected clusters with known WL mass was studied in Sereno et al. (2015) and Sereno & Ettori (2015a), which retrieved a Y_{500}–M_{500} in agreement with self-similar predictions, with an intrinsic scatter of 10 ± 5 per cent on the SZ mass proxy.

The tension between the lower values of the power spectrum amplitude σ_8 inferred from clusters counts (Planck Collaboration et al. 2016c, $\sigma_8 \sim 0.71$–0.78 and references therein) and higher estimates from measurements of the primary Cosmic Microwave Background (CMB) temperature anisotropies (Planck Collaboration et al. 2016b, $\sigma_8 = 0.83 \pm 0.02$) may be due to the Y_{500}–M_{500} relation used to estimate cluster masses. Consistency can be achieved if *Planck* masses, which are based on SZ/X-ray proxies (Planck Collaboration et al. 2014a,b), are biased low by ∼ 40 per cent (Planck Collaboration et al. 2016c).

The level of bias has to be assessed but it is still debated. Gruen et al. (2014) presented the WL analysis of 12 SZ selected clusters, including 5 *Planck* clusters. The comparison of WL masses and Compton parameters showed significant discrepancies correlating with cluster mass or redshift. Comparing the *Planck* masses to the WL masses of the WtG clusters (Weighing the Giants; Applegate et al. 2014), von der Linden et al. (2014b) found evidence for a significant mass bias and a mass dependence of the calibration ratio. The analysis of the CCCP clusters (Canadian Cluster Comparison Project; Hoekstra et al. 2015) confirmed that the bias in the

hydrostatic masses used by the *Planck* team depends on the cluster mass, but with normalization 9 per cent higher than what was found in von der Linden et al. (2014b). Smith et al. (2016) found that the mean ratio of the *Planck* mass estimate to LoCuSS (Local Cluster Substructure Survey) lensing mass is 0.95 ± 0.04.

An unambiguous interpretation of the bias dependence in terms of either redshift or masses can be hampered by the small sample size. Exploiting a large collection of WL masses, Sereno et al. (2015) and Sereno & Ettori (2017) found the bias to be redshift rather than mass dependent.

Even though some of the disagreement among competing analyses can de due to statistical methodologies not properly accounting for Eddington/Malmquist biases and evolutionary effects, see discussion in Sereno et al. (2015), Sereno & Ettori (2015a) and Sereno & Ettori (2017), the mass biases found for different cluster samples do not necessarily have to agree. Different samples cover different redshift and mass ranges, where the bias can differ. Furthermore, WL masses are usually available for the most massive clusters only.

In this paper, we perform a WL analysis of a statistically complete and homogeneous subsample of the *Planck* detected clusters, the PSZ2LenS. We analyse all the *Planck* candidate clusters in the fields of two public lensing surveys, the CFHTLenS (Canada France Hawaii Telescope Lensing Survey; Heymans et al. 2012) and the RCSLenS (Red Cluster Sequence Lensing Survey; Hildebrandt et al. 2016), which shared the same observational instrumentation and the same data-analysis tools. PSZ2LenS is homogeneous in terms of selection, observational set-up, data reduction and data analysis.

The paper is structured as follows. In Section 2, we present the main properties of the lensing surveys and the available data. In Section 3, we introduce the second *Planck* Catalogue of SZ Sources (PSZ2; Planck Collaboration et al. 2016a) and the PSZ2LenS sample. In Section 4, we cover the basics of the WL theory. Section 5 is devoted to the selection of the lensed source galaxies. In Section 6, we detail how we modelled the lenses. The strength of the WL signal of the PSZ2Lens clusters is discussed in Section 7. The Bayesian method used to analyse the lensing shear profiles is illustrated in Section 8. The recovered cluster masses and their consistency with previous results are presented in Section 9. In Section 10, we measure the mass–concentration relation of the PSZ2LenS clusters. Section 11 is devoted to the analysis of the stacked signal. In Section 12, we estimate the bias of the *Planck* masses. A discussion of potential systematics effects and residual statistical uncertainties is presented in Section 13. Candidate clusters which were not visually confirmed are discussed in Section 14. Section 15 is devoted to some final considerations. In Appendix A, we discuss the optimal radius to be associated with the recovered shear signal. Appendix B details the lensing weighted average of cluster properties. Appendix C discusses pros and cons of some statistical estimators used for the WL mass.

1.1 Notations and conventions

As a reference cosmological model, we assumed the concordance flat ΛCDM (Λ and Cold Dark Matter) universe with density parameter $\Omega_M = 0.3$, Hubble constant $H_0 = 70\,\mathrm{km s^{-1} Mpc^{-1}}$ and power spectrum amplitude $\sigma_8 = 0.8$. When H_0 is not specified, h is the Hubble constant in units of $100\,\mathrm{km s^{-1} Mpc^{-1}}$.

Throughout the paper, O_Δ denotes a global property of the cluster measured within the radius r_Δ, which encloses a mean overdensity of Δ times the critical density at the cluster redshift, $\rho_{cr} = 3H(z)^2/(8\pi G)$, where $H(z)$ is the redshift-dependent

Hubble parameter and G is the gravitational constant. We also define $E_z \equiv H(z)/H_0$.

The notation 'log' is the logarithm to base 10 and 'ln' is the natural logarithm. Scatters in natural logarithm are quoted in percentage.

Typical values and dispersions of the parameter distributions are usually computed as bi-weighted estimators (Beers, Flynn & Gebhardt 1990) of the marginalized posterior distributions.

2 LENSING DATA

We exploited the public lensing surveys CFHTLenS and RCSLenS. In the following, we introduce the data sets.

2.1 The CFHTLenS

The CFHTLS (Canada France Hawaii Telescope Legacy Survey) is a photometric survey performed with MegaCam. The wide survey covers four independent fields for a total of $\sim$154 deg^2 in five optical bands u^*, g, r, i and z (Heymans et al. 2012).

The survey was specifically designed for WL analysis, with the deep i-band data taken in sub-arcsecond seeing conditions (Erben et al. 2013). The total unmasked area suitable for lensing analysis covers 125.7 deg^2. The raw number density of lensing sources, including all objects that a shape was measured for, is 17.8 galaxies arcmin^{-2} (Hildebrandt et al. 2016). The weighted density is 15.1 galaxies arcmin^{-2}.

The CFHTLenS team provided[1] WL data processed with THELI (Erben et al. 2013) and shear measurements obtained with LENSFIT (Miller et al. 2013). The photometric redshifts were measured with accuracy $\sigma_{z_{\rm phot}} \sim 0.04(1 + z)$ and a catastrophic outlier rate of about 4 per cent (Hildebrandt et al. 2012; Benjamin et al. 2013).

2.2 The RCSLenS

The RCSLenS is the largest public multiband imaging survey to date which is suitable for weak gravitational lensing measurements[2] (Hildebrandt et al. 2016).

The parent survey, i.e. the Red-sequence Cluster Survey 2 (Gilbank et al. 2011, RCS2), is a sub-arcsecond seeing, multiband imaging survey in the *griz* bands initially designed to optically select galaxy cluster. The RCSLenS project later applied methods and tools already developed by CFHTLenS for lensing studies.

The survey covers a total unmasked area of 571.7 deg^2 down to a magnitude limit of $r \sim 24.3$ (for a point source at 7σ). Photometric redshifts based on four-band (g, r, i, z) data are available for an unmasked area covering 383.5 deg^2, where the raw (weighted) number density of lensing sources is 7.2 (4.9) galaxies arcmin^{-2}. The survey area is divided into 14 patches, the largest being 10×10 deg^2 and the smallest being 6×6 deg^2.

Full details on imaging data, data reduction, masking, multicolour photometry, photometric redshifts, shape measurements, tests for systematic errors and the blinding scheme to allow for objective measurements can be found in Hildebrandt et al. (2016).

The RCSLenS was observed with the same telescope and camera as CFHTLS and the project applied the same methods and tools

developed for CFHTLenS. The two surveys share the same observational instrumentation and the same data-analysis tools, which make the shear and the photo-z catalogues highly homogeneous, but some differences can be found in the two data sets.

CFHTLenS features the additional u band and the co-added data are deeper by $\sim$1mag. The CFHTLenS measured shapes of galaxies in the i band. On the other side, since the i band covers only $\sim$70 per cent of the RCS2 area, the r band was used in RCSLenS for shape measurements because of the longest exposure time and the complete coverage.

2.3 Ancillary data

When available, we exploited ancillary data sets to strengthen the measurement of photometric redshifts and secure the selection of background galaxies. For some fields partially covering CFHTLS-W1 and CFHTLS-W4, we complemented the CFHTLenS data with deep near-ultraviolet (near-UV) and near-infrared (near-IR) observations, supplemented by secure spectroscopic redshifts. The full data set of complementary observations was presented and fully detailed in Coupon et al. (2015), who analysed the relationship between galaxies and their host dark matter haloes through galaxy clustering, galaxy–galaxy lensing and the stellar mass function. We refer to Coupon et al. (2015) for further details.

2.3.1 Spectroscopic data

When available, we used the spectroscopic redshifts collected from public surveys by Coupon et al. (2015) instead of the photometric redshift value. Coupon et al. (2015) exploited four main spectroscopic surveys to collect 62220 unique galaxy spectroscopic redshifts with the highest confidence flag.

The largest spectroscopic sample within the W1 area comes from the VIMOS (VIsible MultiObject Spectrograph) Public Extragalactic Survey (VIPERS; Garilli et al. 2014), designed to study galaxies at $0.5 \lesssim z \lesssim 1.2$. The designed survey covers a total area of 16 deg^2 in the W1 field and 8 deg^2 in the W4 field. The first public data release includes redshifts for 54 204 objects (30 523 in VIPERS-W1). Coupon et al. (2015) considered only the galaxies with the highest confidence flags between 2.0 and 9.5.

The VIMOS-VLT (Very Large telescope) Deep Survey (VVDS; Le Fèvre et al. 2005) and the Ultra-Deep Survey (Le Fèvre et al. 2015) cover a total area of 0.75 deg^2 in the VIPERS-W1 field. Coupon et al. (2015) also used the VIMOS-VLT F22 Wide Survey with 12 995 galaxies over 4 deg^2 down to $i < 22.5$ in the southern part of the VIPERS-W4 field (Garilli et al. 2008). In total, Coupon et al. (2015) collected 5122 galaxies with secure flag 3 or 4.

The PRIsm MUlti-object Survey (PRIMUS; Coil et al. 2011) consists of low-resolution spectra. Coupon et al. (2015) retained the 21 365 galaxies with secure flag 3 or 4.

The SDSS-BOSS spectroscopic survey based on data release DR10 (Ahn et al. 2014) totals 4675 galaxies with ZWARNING=0 within the WIRCam area (see below).

2.3.2 The near-IR observations

Coupon et al. (2015) conducted a K_s-band follow-up of the VIPERS fields with the WIRCam instrument at CFHT. Noise correlation introduced by image resampling was corrected exploiting data from

---

[1] The public archive is available through the Canadian Astronomy Data Centre at http://www.cfht.hawaii.edu/Science/CFHLS.

[2] The data products are publicly available at http://www.cadc-ccda.hia-iha.nrc-cnrc.gc.ca/en/community/rcslens/query.html.

the deeper UKIDSS Ultra Deep Survey ($K < 24.5$; Lawrence et al. 2007). Sample completeness reaches 80 per cent at $K_s = 22$.

Coupon et al. (2015) also used the additional data set from the WIRCam Deep Survey data (Bielby et al. 2012), a deep patch of $0.49\,\mathrm{deg}^2$ observed with WIRCam *J*, *H* and K_s bands.

The corresponding effective area in the CFHTLS after rejection for poor WIRCam photometry and masked CFHTLenS areas covers $\sim23.1\,\mathrm{deg}^2$, divided into 15 and $\sim8.1\,\mathrm{deg}^2$ in the VIPERS-W1 and VIPERS-W4 fields, respectively. WIRCAM sources were matched to the optical counterparts based on position.

2.3.3 The UV-GALEX observations

UV deep imaging photometry from the *GALEX* satellite (Martin et al. 2005) is also available for some partial area. Coupon et al. (2015) considered the observations from the Deep Imaging Survey. All *GALEX* pointings were observed with the NUV channel and cover ~10.8 and $\sim1.9\,\mathrm{deg}^2$ of the WIRCam area in VIPERS-W1 and VIPERS-W4, respectively. FUV observations are available for 10 pointings in the central part of W1.

3 THE PSZ2LENS

The second *Planck* Catalogue of Sunyaev–Zel'dovich Sources (PSZ2; Planck Collaboration et al. 2016a) exploits the 29-month full-mission data. The catalogue contains 1653 candidate clusters and it is the largest, all-sky, SZ-selected sample of galaxy clusters yet produced[3].

Only candidates with an SNR (signal-to-noise ratio) above 4.5 detected outside the highest-emitting Galactic regions, the Small and Large Magellanic Clouds and the point source masks were included. Out of the total, 1203 clusters are confirmed with counterparts identified in external optical or X-ray samples or by dedicated follow-ups. The mean redshift is $z \sim 0.25$ and the farthest clusters were found at $z \lesssim 1$, which makes PSZ2 the deepest all-sky catalogue of galaxy clusters.

The *Planck* team calibrated the masses of the detected clusters with known redshift assuming a best-fitting scaling relation between M_{500} and Y_{500}, i.e. the spherically integrated Compton parameter within a sphere of radius r_{500} (Planck Collaboration et al. 2014b). These masses are denoted as M_{SZ} or $M_{500}^{Y_z}$. The catalogue spans a nominal mass range from $M_{SZ} \sim 0.8 \times 10^{14}$ to $16 \times 10^{14}\,\mathrm{M}_\odot$.

We performed the WL analysis of the clusters centred in the CFHTLenS and RCSLenS fields. Out of the 47 PSZ2 sources within the survey fields, we confirmed 40 clusters by visually inspecting the optical images and identifying the BCGs. Five of these candidate galaxy clusters are located in regions of the RCSLenS where photometric redshifts are not available. Even though these galaxy clusters were clearly identified in the optical images, we could not measure the WL signal since we need photometric redshifts for the selection of background galaxies (see Section 5). These clusters are PSZ2 G054.95-33.39 (PSZ2 index: 221), G055.95-34.89 (225), G081.31-68.56 (349), G082.31-67.00 (354) and G255.51+49.96 (1177).

The final catalogue, PSZ2LenS, includes the confirmed 35 galaxy clusters (out of a total of 41 candidates) located in regions where photometric redshifts are available and are presented in Table 1. The cluster coordinates and redshifts correspond to the BCG. We did not

confirm six candidates. Spectroscopic redshifts were recovered via the SIMBAD Astronomical Database[4] for 30 out of the 35 BCGs. Additional updated redshifts for PSZ2 G053.44-36.25 (212) and G114.39-60.16 (554) were found in Carrasco et al. (2017). For the remaining three clusters, we exploited photometric redshifts. The displacements of the SZ centroid from the BCG are pictured in Fig. 1.

Fifteen clusters out of 35 in PSZ2LenS are part of the cosmological subsample used by the *Planck* team for the analysis of the cosmological parameters with number counts.

We could confirm ~85 per cent of the candidate clusters, in very good agreement with the nominal statistical reliability assessed by the *Planck* team (Planck Collaboration et al. 2016a), who placed a lower limit of 83 per cent on the purity.

The results of our identification process are consistent with the validation process by the *Planck* team (Planck Collaboration et al. 2016a), who performed a multiwavelength search for counterparts in ancillary radio, microwave, infra-red, optical and X-ray data sets. 33 out of the 41 candidates were validated by the *Planck* team. This subset shares 32 clusters with PSZ2LenS. There are only a few different assessments by the independent selection processes. We did not include PSZ2 G006.84+50.69 (25), which we identified as a substructure of PSZ2 G006.49+50.56 (21), i.e. Abell 2029 (see Section 14). On the other hand, we included PSZ2 G058.42-33.50 (243), PSZ2 G198.80-57.57 (902) and PSZ2 G211.31-60.28 (955), which were not validated by the *Planck* team.

Since we took all the *Planck* clusters without any further restriction, the lensing clusters constitute an unbiased subsample of the full catalogue. This is a strength of our sample with respect to other WL selected collections, which usually sample only the massive end of the full population (see discussion in Sereno et al. 2015).

The mass and redshift distribution of PSZ2LenS is representative of the full population of *Planck* clusters; see Figs 2, 3 and 4. According to the Kolmogorov–Smirnov test, there is a 53 per cent probability that the masses of our WL subsample and of the full sample are drawn from the same distribution. The redshift distributions are compatible at the 96 per cent level.

The cluster catalogue and the shape measurements are extracted from completely different data sets, the PSZ2-Survey and CFHTLenS/RCSLenS data, respectively. The distribution of lenses is then uncorrelated with residual systematics in the shape measurements (Miyatake et al. 2015).

4 WL SHEAR

The reduced tangential shear g_+ is related to the differential projected surface density $\Delta\Sigma_+$ of the lenses (Mandelbaum et al. 2013; Velander et al. 2014; Viola et al. 2015). For a single source redshift,

$$\Delta\Sigma_+(R) = \gamma_+ \Sigma_{cr} = \bar{\Sigma}(<R) - \Sigma(R), \tag{1}$$

where Σ is the projected surface density and Σ_{cr} is the critical density for lensing,

$$\Sigma_{cr} = \frac{c^2}{4\pi G}\frac{D_s}{D_d D_{ds}}, \tag{2}$$

where c is the speed of light in vacuum, G is the gravitational constant and D_d, D_s and D_{ds} are the angular diameter distances to the lens, to the source, and from the lens to the source, respectively.

Table 1. The PSZ2LenS sample. Column 1: cluster name. Column 2: index in the PSZ2-Union catalogue. Columns 3 and 4: right ascension and declination in degrees (J2000) of the associated BCG. Column 5: redshift. A star indicates a photometric redshift. Column 7: lensing survey. Column 8: survey patch. The suffix NIR means that ancillary data were available.

| PSZ2	Index	RA	DEC	z	Survey	Field
G006.49+50.56	21	227.733767	5.744914	0.078	RCSLenS	1514
G011.36+49.42	38	230.466125	7.708881	0.044	RCSLenS	1514
G012.81+49.68	43	230.772096	8.609181	0.034	RCSLenS	1514
G053.44-36.25	212	323.800386	−1.049615	0.327	RCSLenS	2143
G053.63-41.84	215	328.554600	−3.998100	0.151	RCSLenS	2143
G053.64-34.48	216	322.416475	0.089100	0.234	RCSLenS	2143
G058.42-33.50	243	323.883680	3.867200	0.400*	RCSLenS	2143
G059.81-39.09	251	329.035737	1.390939	0.222	RCSLenS	2143
G065.32-64.84	268	351.332080	−12.124360	0.082	RCSLenS	2338
G065.79+41.80	271	249.715656	41.626982	0.336	RCSLenS	1645
G077.20-65.45	329	355.320925	−9.019929	0.251	RCSLenS	2338
G083.85-55.43	360	351.882792	0.942811	0.279	RCSLenS	2329
G084.69+42.28	370	246.745833	55.474961	0.140	RCSLenS	1613
G087.03-57.37	391	354.415650	0.271253	0.277	RCSLenS	2329
G096.14+56.24	446	218.868592	55.131111	0.140	CFHTLenS	W3
G098.44+56.59	464	216.852112	55.750253	0.141	CFHTLenS	W3
G099.48+55.60	473	217.159762	56.860909	0.106	CFHTLenS	W3
G099.86+58.45	478	213.696611	54.784321	0.630*	CFHTLenS	W3
G113.02-64.68	547	8.632500	−2.115100	0.081	RCSLenS	0047
G114.39-60.16	554	8.617292	2.423011	0.384	RCSLenS	0047
G119.30-64.68	586	11.302080	−1.875440	0.545	RCSLenS	0047
G125.68-64.12	618	14.067088	−1.255492	0.045	RCSLenS	0047
G147.88+53.24	721	164.379271	57.995912	0.528	RCSLenS	1040
G149.22+54.18	724	164.598600	56.794931	0.135	RCSLenS	1040
G150.24+48.72	729	155.836579	59.810944	0.199	RCSLenS	1040
G151.62+54.78	735	163.722100	55.350600	0.470	RCSLenS	1040
G167.98-59.95	804	33.671129	−4.567300	0.140	CFHTLenS	W1-NIR
G174.40-57.33	822	37.920500	−4.882580	0.185	CFHTLenS	W1-NIR
G198.80-57.57	902	45.527500	−15.561800	0.350*	RCSLenS	0310
G211.31-60.28	955	45.302332	−22.549510	0.400*	RCSLenS	0310
G212.25-53.20	956	52.774492	−21.009075	0.188	RCSLenS	0310
G212.93-54.04	961	52.057408	−21.672833	0.600	RCSLenS	0310
G230.73+27.70	1046	135.377830	−1.654880	0.294	CFHTLenS	W2
G233.05+23.67	1057	133.065400	−5.567200	0.192	CFHTLenS	W2
G262.95+45.74	1212	165.881133	−8.586525	0.154	RCSLenS	1111
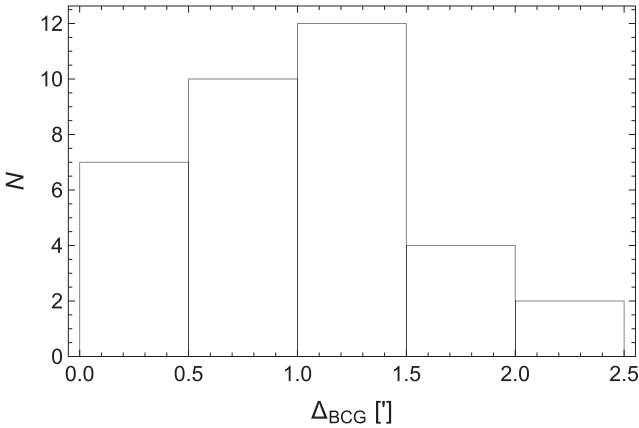
Figure 1. Distribution of displacements between SZ centroid and BCG in the PSZ2LenS sample. Displacements are in units of arcminutes.
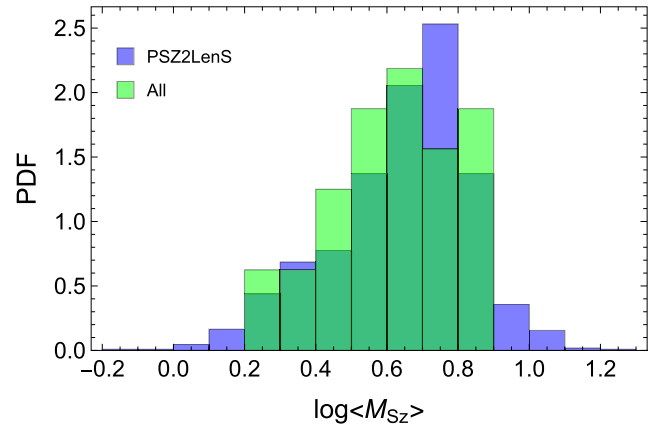

Figure 2. The mass distribution of the *Planck* clusters. The histograms are rescaled to unitary area and show the distribution in mass of all the PSZ2 clusters with identified counterpart (green) and the PSZ2LenS subsample in the fields of the CFHTLenS/RCSLenS (blue). The masses are in units of $10^{14}\,\mathrm{M_\odot}$.
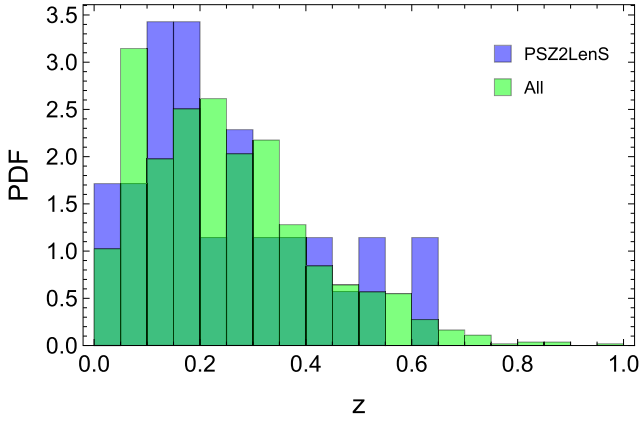
Figure 3. The redshift distribution of the *Planck* clusters. The histograms are rescaled to unitary area and show the distribution in redshift of all the PSZ2 clusters with identified counterpart (green) and the PSZ2LenS subsample in the fields of the CFHTLenS/RCSLenS (blue).
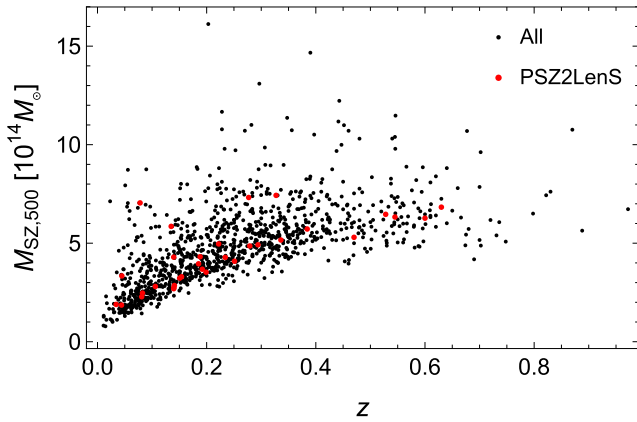

Figure 4. Distribution of the PSZ2 clusters with known redshift in the M_{SZ}-z plane. The black and red points denote all the PSZ2 clusters with an identified counterpart and the PSZ2LenS subsample in the fields of the CFHTLenS/RCSLenS, respectively.

The signal behind the clusters can be extracted by stacking in circular annuli as

$$\Delta\Sigma_+(R) = \frac{\sum_i (w_i\,\Sigma_{cr,i}^{-2})\epsilon_{+,i}\,\Sigma_{cr,i}}{\sum_i (w_i\,\Sigma_{cr,i}^{-2})}, \tag{3}$$

where $\epsilon_{+,i}$ is the tangential component of the ellipticity of the *i*-th source galaxy after bias correction and w_i is the `lensfit` weight assigned to the source ellipticity. The sum runs over the galaxies included in the annulus at projected distance R.

If the redshifts are known with an uncertainty, as it is the case for photometric redshifts, the point estimator in equation (3) is biased. Optimal estimators exploiting the full information contained in the probability density distribution of the photometric redshift have been advocated (Sheldon et al. 2004), but these methods can be hampered by the uncertain determination of the shape of the probability distribution, which is very difficult to ascertain (Tanaka et al. 2017). However, the level of systematics introduced by the estimator in equation (3) for quality photometric redshifts as those of the CFHTLens/RCSLenS is under control and well below the statistical uncertainty; see Section 13.6. We can safely use it in our analysis.

The raw ellipticity components, $e_{m,1}$ and $e_{m,2}$, were calibrated and corrected by applying a multiplicative and an additive correction,

$$e_{true,i} = \frac{e_{m,i} - c_i}{1 + \bar{m}} \qquad (i = 1, 2)\,. \tag{4}$$

The bias parameters can be estimated either from simulated images or empirically from the data.

The multiplicative bias m was identified from the simulated images (Heymans et al. 2012; Miller et al. 2013). The simulation-based estimate mostly depends on the shape measurement technique and is common to both CFHTLenS and RCSLenS. In each sky area, we considered the average $\bar{m}$, which was evaluated taking into account the weight of the associated shear measurement (Viola et al. 2015),

$$\bar{m}(R) = \frac{\sum_i w_i\,\Sigma_{cr,i}^{-2}m_i}{\sum_i w_i\,\Sigma_{cr,i}^{-2}}. \tag{5}$$

The two surveys suffer for a small but significant additive bias at the level of a few times 10^{-3}. This bias depends on the SNR and the size of the galaxy. The empirical estimate of the additive bias is very sensitive to the actual properties of the data (Heymans et al. 2012; Miller et al. 2013) and it differs in the two surveys (Hildebrandt et al. 2016). The residual bias in the first component is consistent with zero ($c_1 = 0$) for CFHTLenS (Heymans et al. 2012; Miller et al. 2013), which is not the case for RCSLenS (Hildebrandt et al. 2016). Furthermore, RCSLenS had to model the complex behaviour of the additive ellipticity bias with a two-stage process. The first stage is the detector-level correction. Once this is corrected for, the residual systematics attributed to noise bias are removed (Hildebrandt et al. 2016).

5 BACKGROUND SELECTION

Our source galaxy sample includes all detected galaxies with a non-zero shear weight and a measured photometric redshift (Miller et al. 2013). We did not reject those pointings failing the requirements for cosmic shear but still suitable for galaxy lensing (Velander et al. 2014; Coupon et al. 2015).

Our selection of background galaxies relies on robust photometric redshifts. Photometric redshifts exploiting the ancillary data sets were computed in Coupon et al. (2015) with the template fitting code `LEPHARE` (Ilbert et al. 2006). The spectroscopic sample described in Section 2.3.1 was used for validation and calibration. These photometric redshifts were retrieved within a dispersion ∼0.03–0.04(1 + z) and feature a catastrophic outlier rate of ∼1–4 per cent. Main improvements with respect to CFHTLenS rely on the choice of isophotal magnitudes and PSF homogenization (Hildebrandt et al. 2012) at faint magnitude, and the contribution of NIR data above $z \sim 1$. The UV photometry improves the precision of photometric redshifts at low redshifts, $z \lesssim 0.2$.

As a preliminary step, we identified (as candidate background sources for the WL analysis behind the lens at z_{lens}) galaxies such that

$$z_s > z_{lens} + \Delta z_{lens}, \tag{6}$$

where z_s is the photometric redshift or, if available, the spectroscopic redshift. For our analysis, we conservatively set $\Delta z_{lens} = 0.05$. On top of this minimal criterion, we required that the sources passed more restrictive cuts in either photometric redshift or colour properties, which we discuss in the following.
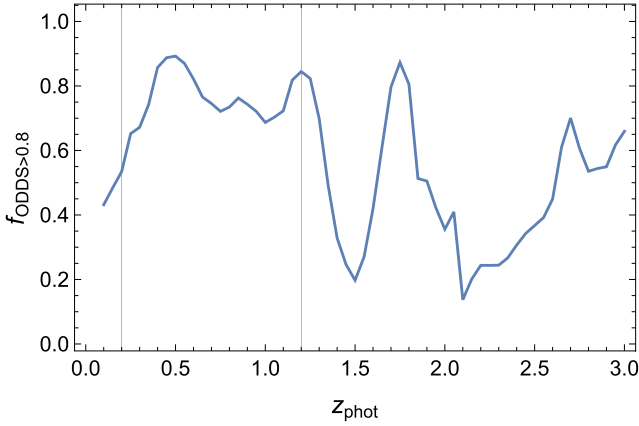
Figure 5. Fraction of galaxies in the W1 field of the CFHTLenS catalogue with ODDS ≥ 0.8 as a function of the photometric redshift. Here, redshift estimates exploit the optical *ugriz* bands. The vertical red lines delimit the allowed redshift range for CFHTLenS sources.

5.1 Photometric redshifts

As a first additional criterion for galaxies with either spectroscopic redshifts or photometric redshift, z_s, we adopted the cuts

$$z_{2.3\,\%} > z_{\text{lens}} + \Delta z_{\text{lens}} \quad \text{AND} \quad z_{\min} < z_s < z_{\max}, \tag{7}$$

where $z_{2.3\,\text{per cent}}$ is the lower bound of the region including the 2σ (95.4 per cent) of the probability density distribution, i.e. there is a probability of 97.7 per cent that the galaxy redshift is higher than $z_{2.3\,\text{per cent}}$. The redshifts $z_{\min}$ and $z_{\max}$ are the lower and upper limits of the allowed redshift range, respectively.

For the galaxies with spectroscopic redshift, $z_{\min} = 0$ whereas $z_{\max}$ is arbitrarily large. For the sample with only photometric redshifts, the allowed redshift range was determined according to the available bands. For the galaxies exploiting only the CFHTLenS photometry (*ugriz*), we restricted the selection to $0.2 < z_{\text{phot}} < 1.2$; for the RCSLenS photometric redshifts, which lack for the *u* band, we restricted the selection to $0.4 < z_{\text{phot}} < 1.2$; for galaxies with additional NIR data, we relaxed the upper limit, i.e. we set $z_{\max}$ to be arbitrarily large; for galaxies with ancillary UV data, we relaxed the lower limit, i.e. we set $z_{\min} = 0$.

In case of only optical filters without NIR data, we required that the posterior probability distribution of the photometric redshift is well behaved by selecting galaxies whose fraction of the integrated probability included in the primary peak exceeds 80 per cent,

$$\text{ODDS} \geq 0.8. \tag{8}$$

The ODDS parameter quantifies the relative importance of the most likely redshift (Hildebrandt et al. 2012). The additional selection criterion based on the ODDS parameter guarantees for a clean selection but it is somewhat redundant. In fact, most of the galaxies with ODDS < 0.8 were already cut by retaining only galaxies in the redshift range $z_{\min} < z < z_{\max}$ (see Fig. 5). For sources in the CFHTLenS without ancillary information, a fraction of ~ 76 per cent of the sources in the redshift range $0.2 < z < 1.2$ meet the ODDS requirement.

By definition, the constraint $z_{2.3\,\text{per cent}} > z_{\text{lens}}$ guarantees that the contamination is at the 2.3 per cent level. The additional Δz_{lens} requirement in equation (7) makes the contamination even lower. Since $\Delta z_{\text{lens}} = 0.05$ is $\sim 1(0.5)\sigma_{\text{phot}}$ at $z_s = 0.2(1.2)$, we are practically requiring that the contamination is ~ 0.1 (0.6) per cent for galaxies at $z_{\text{phot}} = 0.2(1.2)$.
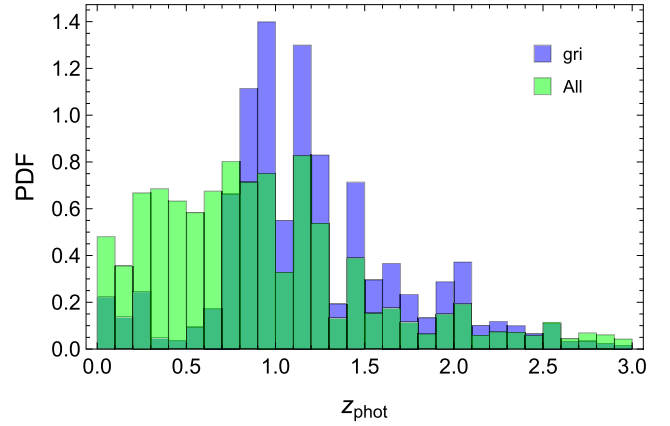

Figure 6. Photometric redshift distributions of galaxies in the COSMOS catalogue, before (green) and after (blue) the *gri* colour–colour cut.

When available, the impact of ancillary UV and mainly NIR data is significant. Thanks to the increased accuracy in the redshift estimates, we can include in the background sample more numerous and more distant galaxies. In particular, when we could rely on improved photometric redshift estimates based on the NIR additional data set, we did not have to restrict our redshift sample to $z_{\text{phot}} < 1.2$, increasing the full background source sample by ~ 30 per cent compared to other CFHTLenS lensing studies, without introducing any systematic bias (Coupon et al. 2015).

5.2 Colour–colour space

The population of source galaxies can be identified with a colour–colour selection (Medezinski et al. 2010; Formicola et al. 2016). For clusters at $z_{\text{lens}} < 0.65$, we adopted the following criterion exploiting the *gri* bands, which efficiently select galaxies at $z_s \gtrsim 0.7$ (Oguri et al. 2012; Covone et al. 2014):

$$(g - r < 0.3) \quad \text{OR} \quad (r - i > 1.3) \quad \text{OR} \quad (r - i > g - r). \tag{9}$$

To pass this cut, lensing sources have to be detected in the *r* band and in at least one of the filters *g* or *i*.

Since we use photometric redshifts to estimate the lensing depth, we required

$$z_s > z_{\min}, \tag{10}$$

as for the z_{phot} selection. The two-colour method may select as background sources an overdensity of sources at low photometric redshifts (Covone et al. 2014). Most of these sources are characterized by a low value of the ODDS parameter, and z_{phot} is not well constrained, hinting to possible degeneracies in the photometric redshift determination based only on optical colours. Since z_{phot} still enters in the estimate of the lensing depth, we conservatively excluded these galaxies through equation (10).

The colour cuts in equation (9) were originally proposed by Oguri et al. (2012) based on the properties of the galaxies in the COSMOS photometric catalogue (Ilbert et al. 2009), which provides very accurate photometric redshifts down to $i \sim 25$. They determined the cuts after inspection of the photometric redshift distributions in the *g–r* versus *r–i* colour space. The criteria are effective; see Fig. 6. When we analyse the distribution of photometric redshifts, 64.4 per cent of the 385 044 galaxies in the COSMOS survey with measured photometric redshift have $z_{\text{phot}} > 0.63$, i.e. the highest cluster redshift in our sample. After the colour–colour cut, 92.0 per cent of the selected galaxies have $z_{\text{phot}} > 0.63$. If we limit the galaxy sample to
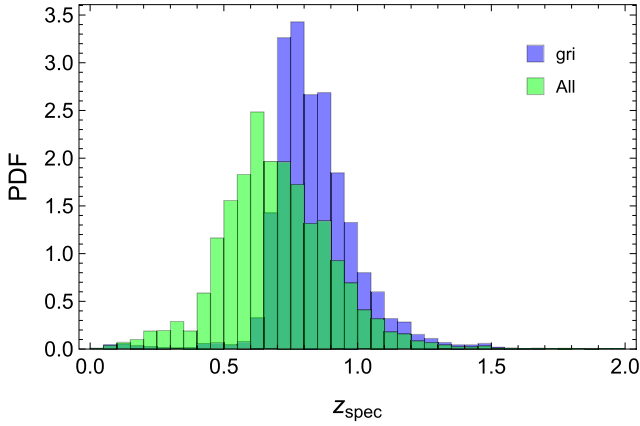
Figure 7. Spectroscopic redshift distributions of VIPERS/VVDS galaxies in CFHTLS-W1, W4, before (green) and after (blue) the *gri* colour–colour cut.

$z_s > 0.2(0.4)$, as required in equation (10), 95.4 (98.3) per cent of the selected galaxies have $z_{phot} > 0.63$. In fact, a very high fraction of the not entitled galaxies which pass the colour test (44.4 per cent) forms an overdensity at $z_{phot} \lesssim 0.2$.

We can further assess the reliability of the colour-space selection considering the spectroscopic samples in CFHTLS-W1 and W4 fields. We considered the 61 525 galaxies from the VIPERS and VVDS samples with high-quality spectroscopic redshifts and good CFHTLS *gri* photometry. Before the cut, 61.6 per cent of the sources have $z_{spec} > 0.63$. After the cut, 97.0 per cent of the 26 711 selected galaxies have $z_{spec} > 0.63$; see Fig. 7. If we only consider galaxies with $z_s > 0.2(0.4)$, as required in equation (10), 97.7 (98.1) per cent of the selected galaxies have $z_{phot} > 0.63$.

Based on the above results, we can roughly estimate that a galaxy passing the *gri* cuts has a $\gtrsim 95$ per cent probability of being at $z > 0.63$. When combined with the constraint $z_{phot} > z_{lens}$, the combined probability of the galaxy of being behind the highest redshift PSZ2LenS cluster goes up to $\gtrsim 98$ per cent.

6 LENS MODEL

The lensing signal is generated by all the matter between the observer and the source. For a single line of sight, we can break the signal down in three main components: the main halo, the correlated matter around the halo, and the uncorrelated matter along the line of sight.

The profile of the differential projected surface density of the lens can then be modelled as

$$\Delta\Sigma_{tot} = \Delta\Sigma_{1h} + \Delta\Sigma_{2h} \pm \Delta\Sigma_{LSS}. \quad (11)$$

The dominant contribution up to $\sim 3\,\mathrm{Mpc}\,h^{-1}$, $\Delta\Sigma_{1h}$, comes from the cluster; the second contribution is the 2-halo term, $\Delta\Sigma_{2h}$, which describes the effects of the correlated matter distribution around the location of the main halo. The 2-halo term is mainly effective at scales $\gtrsim 10\,\mathrm{Mpc}$. $\Delta\Sigma_{LSS}$ is the noise contributed by the uncorrelated matter.

The cluster can be modelled as a Navarro Frenk White (NFW) density profile (Navarro, Frenk & White 1997),

$$\rho_{NFW} = \frac{\rho_s}{(r/r_s)(1 + r/r_s)^2}, \quad (12)$$

where r_s is the inner scale length and ρ_s is the characteristic density. In the following, as a reference halo mass, we consider M_{200}, i.e.

the mass in a sphere of radius r_{200}. The concentration is defined as $c_{200} = r_{200}/r_s$.

The NFW profile may be inaccurate in the very inner region or in the outer region. The action of baryons, the presence of a dominant BCG and deviations from the NFW predictions (Mandelbaum, Seljak & Hirata 2008; Dutton & Macciò 2014; Sereno, Fedeli & Moscardini 2016) can play a role. However, for CFHTLenS/RCSLenS quality data, systematics caused by poor modelling are subdominant with respect to the statistical noise. Furthermore, in the radial range of our consideration, $0.1 < R < 3\,\mathrm{Mpc}\,h^{-1}$, the previous effects are subdominant.

To better describe the transition region between the infalling and the collapsed matter at large radii, the NFW density profile can be smoothly truncated as (Baltz, Marshall & Oguri 2009, BMO),

$$\rho_{BMO} = \rho_{NFW}(r)\left(\frac{r_t^2}{r^2 + r_t^2}\right)^2, \quad (13)$$

where r_t is the truncation radius. For our analysis, we set $r_t = 3\,r_{200}$ (Oguri & Hamana 2011; Covone et al. 2014).

The 2-halo term $\Delta\Sigma_{2h}$ arises from the correlated matter distribution around the location of the galaxy cluster (Covone et al. 2014; Sereno et al. 2015b). The 2-halo shear around a single lens of mass M at redshift z for a single source redshift can be modelled as (Oguri & Takada 2011; Oguri & Hamana 2011)

$$\gamma_{+,2h}(\theta; M, z) = \int \frac{l\,dl}{2\pi} J_2(l\theta) \frac{\bar{\rho}_m(z) b_h(M; z)}{(1 + z)^3 \Sigma_{cr} D_d^2(z)} P_m(k_l; z), \quad (14)$$

where θ is the angular radius, J_n is the Bessel function of n-th order and $k_l \equiv l/[(1 + z)D_d(z)]$. b_h is the bias of the haloes with respect to the underlying matter distribution (Sheth & Tormen 1999; Tinker et al. 2010; Bhattacharya et al. 2013). $P_m(k_l; z)$ is the linear power spectrum. We computed P_m following Eisenstein & Hu (1999), which is fully adequate given the precision needed in our analysis.

The 2-halo term boosts the shear signal at $\sim 10\,\mathrm{Mpc}\,h^{-1}$ but its effect is negligible at $R \lesssim 3\,\mathrm{Mpc}\,h^{-1}$ even in low mass groups (Covone et al. 2014; Sereno et al. 2015b). In order to favour a lens modelling as simple as possible but to still account for the correlated matter, we expressed the halo bias b_h as a known function of the peak eight, i.e. in terms of the halo mass and redshift, as prescribed in Tinker et al. (2010).

The final contribution to the shear signal comes from the uncorrelated large-scale structure projected along the line of sight. We modelled it as a cosmic noise which we added to the uncertainty covariance matrix (Hoekstra 2003). The noise, σ_{LSS}, in the measurement of the average tangential shear in an angular bin ranging from θ_1 to θ_2 caused by a large-scale structure can be expressed as (Schneider et al. 1998; Hoekstra 2003)

$$\sigma_{LSS}^2(\theta_1, \theta_2) = 2\pi \int_0^\infty P_k(l) g^2(l, \theta_1, \theta_2)\, dl, \quad (15)$$

where $P_k(l)$ is the effective projected power spectrum of lensing and the function $g(l, \theta_1, \theta_2)$ embodies the filter function U as

$$g(l, \theta_1, \theta_2) = \int_0^{\theta_2} \phi U(\phi) J_0(l\phi)\, d\phi. \quad (16)$$

The filter of the convergence power spectrum is specified by our choice to consider the azimuthally averaged tangential shear (Hoekstra et al. 2011). The effects of non-linear evolution on the relatively small scales of our interest were accounted for in the power spectrum following the prescription of Smith et al. (2003). We computed σ_{LSS} at the weighted redshift of the source distribution.

Table 2. Background galaxy samples for WL shear measurements. The signal was collected between 0.1 and 3.16 Mpc h^{-1}. Column 1: PSZ2 index of the cluster. Column 2: cluster redshift. Column 3: effective source redshift. Column 4: the total number of background galaxies. Column 5: raw number density of background lensing sources per square arc minute, including all objects with measured shape. Column 6: WL SNR.

Index	z_{lens}	z_{back}	N_g	n_g	SNR
21	0.078	0.712	13 171	1.61	2.71
38	0.044	0.752	71 520	3.02	−0.22
43	0.034	0.728	121 913	3.18	2.26
212	0.327	0.875	2956	3.71	5.71
215	0.151	0.687	2972	1.15	−0.25
216	0.234	0.820	1801	1.40	0.15
243	0.400	0.908	981	1.59	0.09
251	0.222	0.847	3529	2.54	1.92
268	0.082	0.670	22 135	2.99	1.75
271	0.336	0.891	1741	2.26	1.73
329	0.251	0.857	1799	1.56	3.01
360	0.279	0.803	2025	2.04	1.17
370	0.140	0.691	4242	1.45	1.41
391	0.277	0.874	4218	4.21	5.35
446	0.140	0.769	24 930	8.53	4.48
464	0.141	0.755	27 632	9.55	5.45
473	0.106	0.760	53 052	11.24	2.25
478	0.630	0.967	2831	7.43	2.85
547	0.081	0.688	18 122	2.38	2.94
554	0.384	0.909	1303	2.01	2.40
586	0.545	1.156	478	1.09	0.46
618	0.045	0.678	43 093	1.87	4.24
721	0.528	0.880	681	1.51	0.86
724	0.135	0.745	11 376	3.66	6.51
729	0.199	0.791	3530	2.14	1.39
735	0.470	0.921	1247	2.45	1.05
804	0.140	0.758	41 113	14.01	2.57
822	0.185	0.789	19 936	10.80	3.08
902	0.350	0.897	1713	2.35	1.28
955	0.400	1.036	800	1.30	−0.11
956	0.188	0.695	1626	0.90	1.70
961	0.600	1.164	123	0.31	0.26
1046	0.294	0.863	4731	5.13	2.16
1057	0.192	0.777	8209	4.71	5.07
1212	0.154	0.717	2999	1.20	0.93

The cosmic-noise contributions to the total uncertainty covariance matrix can be significant at very large scales or for very deep observations (Umetsu et al. 2014). In our analysis, the source density is relatively low and errors are dominated by the source galaxy shape noise. For completeness, we nevertheless considered the cosmic noise in the total uncertainty budget.

7 LENSING SIGNAL

Our lensing sample consists of all the PSZ2 confirmed clusters centred in the CFHTLenS and RCSLenS fields with photometric redshift coverage. This leaves us with 35 clusters; see Table 1.

The lensing properties of the background galaxy samples used for the WL shear measurements are listed in Table 2. The effective redshift z_{back} of the background population is defined as

$$\eta(z_{back}) = \frac{\sum_i w_i \eta_i}{\sum_i w_i}, \tag{17}$$

where $\eta = D_{ds}D_d/D_s$. The effective source redshift characterizes the background population. We did not use it in the fitting procedure, where we analysed the differential surface density derived
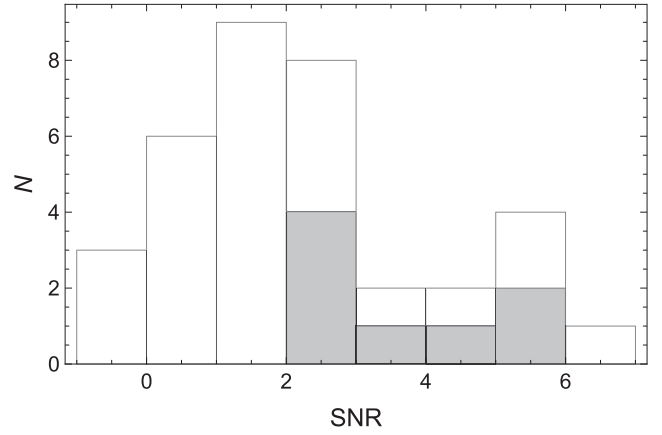

Figure 8. Distribution of the SNR of the shear signal of the PSZ2LenS clusters. The white and grey histograms show the combined RCSLenS plus CFHTLenS or the CFHTLenS sample only, respectively.
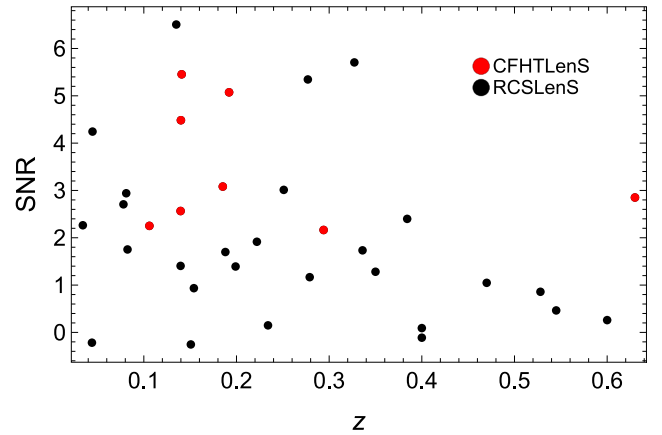

Figure 9. SNR of the shear signal versus the cluster redshift of the PSZ2LenS clusters. The red and black points show the RCSLenS and the CFHTLenS sample, respectively.

by considering the individual redshifts of the selected background galaxies; see equation (3).

We define the total signal of the detection as the weighted differential density between 0.1 and 3.16 Mpc h^{-1}, $\langle \Delta \Sigma_+ \rangle_{0.1 < R < 3}$. The SNR is then

$$\text{SNR} = \frac{\langle \Delta \Sigma_+ \rangle_{0.1 < R < 3}}{\delta_+}, \tag{18}$$

where δ_+ is the statistical uncertainty.

The distribution of SNR is shown in Fig. 8. Nine (17) clusters out of 35 sport an SNR in excess of 3 (2). Three clusters exhibit a negative signal. Since we measured the SNR in a fixed physical size, low redshift clusters, which cover a larger area of the sky, were detected with a higher precision; see Fig. 9.

Due to the deeper observations, clusters in the fields of the CFHTLenS have larger SNRs at a given mass and redshift. The median SNR for the CFHTLenS is 3.0, whereas for the RCSLenS clusters it is 1.4. This does not bias our analysis since the subsample of PSZ2LenS in the fields of the CFHTLenS is an unbiased sample of the full PSZ2 catalogue by itself. On the other hand, the survey area of the RCSLenS is three times larger than the CFHTLenS, which counterbalances the smaller number density of background sources as far as the total signal is concerned.

8 INFERENCE

In our reference scheme, the lens is characterized by two free parameters, the mass and the concentration, which we determined by fitting the shear profile. We performed a standard Bayesian analysis (Sereno et al. 2015a). The posterior probability density function of mass M_{200} and concentration c_{200} given the data $\{\Delta\Sigma_+\}$ is

$$p(M_{200}, c_{200}|\{\Delta\Sigma_+\}) \propto \mathcal{L}(M_{200,c_{200}})p_{\mathrm{prior}}(M_{200})p_{\mathrm{prior}}(c_{200}), \quad (19)$$

where $\mathcal{L}$ is the likelihood and p_{prior} represents a prior.

8.1 Likelihood

The likelihood can be expressed as $\mathcal{L} \propto \exp(-\chi^2)$, where the χ^2 function can be written as

$$\chi^2 = \sum_i \left[\frac{\Delta\Sigma_+(R_i) - \Delta\Sigma_+(R_i; M_{200}, c_{200})}{\delta_+(R_i)} \right]^2 ; \quad (20)$$

the sum extends over the radial annuli and the effective radius R_i of the i-th bin is estimated as a shear-weighted radius, see Appendix A; $\Delta\Sigma_+(R_i)$ is the differential surface density in the annulus and $\delta_+(R_i)$ is the corresponding uncertainty also accounting for cosmic noise.

The differential surface density $\Delta\Sigma_+$ was measured between 0.1 and ~ 3.16 Mpc h^{-1} from the cluster centre in 15 radial circular annuli equally distanced in logarithmic space. The binning is such that there are 10 bins per decade, i.e. 10 bins between 0.1 and 1 Mpc h^{-1}. The use of the shear-weighted radius makes the fitting procedure stabler with respect to radial binning; see Appendix A.

The tangential and cross components of the shear were computed from the weighted ellipticity of the background sources as described in Section 4.

In our reference fitting scheme, we modelled the lens with a BMO profile; alternatively, we adopted the simpler NFW profile.

8.2 Priors

The probabilities $p_{\mathrm{prior}}(M_{200})$ and $p_{\mathrm{prior}}(c_{200})$ are the priors on mass and concentration, respectively. Mass and concentration of massive haloes are expected to be related. *N*-body simulations and theoretical models based on the mass accretion history show that concentrations are higher for lower mass haloes and are smaller at early times (Bullock et al. 2001; Duffy et al. 2008; Zhao et al. 2009; Giocoli, Tormen & Sheth 2012). A flattening of the *c*–*M* relation is expected to occur at higher masses and redshifts (Klypin, Trujillo-Gomez & Primack 2011; Prada et al. 2012; Meneghetti & Rasia 2013; Dutton & Macciò 2014; Ludlow et al. 2014; Diemer & Kravtsov 2015).

Selection effects can preferentially include overconcentrated clusters which deviate from the mean relation. This effect is very significant in lensing selected samples but can survive to some extent even in X-ray selected samples (Meneghetti et al. 2014; Sereno et al. 2015a). Orientation effects hamper the lensing analysis. As an example, the concentration measured under the assumption of spherical symmetry can be strongly overestimated for triaxial clusters aligned with the line of sight.

In our reference inference scheme, we then considered both mass and concentration as uncorrelated a priori. As prior for mass and concentration, we considered uniform probability distributions in the ranges $0.05 \leq M_{200}/(10^{14}h^{-1}\,\mathrm{M}_\odot) \leq 100$ and $1 \leq c_{200} \leq 20$, respectively, with the distributions being null otherwise.

There are some main advantages with this non-informative approach: (i) the flexibility associated with the concentration can accommodate deviations of real clusters from the simple NFW modelling; (ii) we can deal with selection effects and apparent very large values of c_{200}; (iii) lensing estimates of mass and concentration are strongly anticorrelated and a misleading strong prior on the concentration can bias the mass estimate; (iv) the mass–concentration relation is cosmology dependent with overconcentrated clusters preferred in universes with high values of σ_8. Since the value of σ_8 is still debated (Planck Collaboration et al. 2016c), it can be convenient to relax the assumption on σ_8 and on the *c*–*M* relation.

As an alternative set of priors, we adopted uniform distributions in logarithmically spaced intervals, as suitable for positive parameters (Sereno & Covone 2013): $p_{\mathrm{prior}}(M_{200}) \propto 1/M_{200}$ and $p_{\mathrm{prior}}(c_{200}) \propto 1/c_{200}$ in the allowed ranges and null otherwise. These priors avoid the bias of the concentration towards large values that can plague lensing analysis of good-quality data (Sereno & Covone 2013). On the contrary, in shallow surveys such as the RCSLenS, these priors can bias low the estimates of mass and concentration.

As a third prior for the concentration, we considered a lognormal distribution with median value $c_{200} = 4$ and scatter of 0.7 in natural logarithms. As before, we considered hard limits $1 < c_{200} < 20$. The median value of the prior is approximately what found for massive clusters in numerical simulations. The scatter is nearly two times what is found for the mass–concentration relation (Bhattacharya et al. 2013; Meneghetti et al. 2014).

We did not leave the halo bias as a free parameter, i.e. the prior on the bias is a Dirac delta function δ. In the reference scheme, the 1-halo term is described with a BMO profile and the halo bias is computed as a function of the peak height ν, $b_{\mathrm{h}} = b_{\mathrm{h}}[\nu(M_{200}, z)]$, as described in Tinker et al. (2010). When we alternatively model the main halo as a NFW profile, we set $b_{\mathrm{h}} = 0$.

9 WL MASSES

Results of the regression procedure for the reference settings of priors are listed in Table 3. Virial overdensities, Δ_{vir}, are based on the spherical collapse model and are computed as suggested in Bryan & Norman (1998).

Some *Planck* clusters in CFHTLenS and RCSLenS have been the subject of other WL studies in the past. We collected previous results from the Literature Catalogs of weak Lensing Clusters of galaxies (LC²), the largest compilations of WL masses up to date[5] (Sereno 2015). LC² are standardized catalogues comprising 879 (579 unique) entries with measured WL mass retrieved from 81 bibliographic sources.

We identified counterparts in the LC² catalogue by matching cluster pairs whose redshifts differ for less than $\Delta z = 0.1$ and whose projected distance in the sky does not exceed 0.5 Mpc h^{-1}.

12 PSZ2LenS clusters have already been studied in previous analyses by Dahle et al. (2002); Dahle (2006); Gruen et al. (2014); Hamana et al. (2009); Kettula et al. (2015); Cypriano et al. (2004); Merten et al. (2015); Okabe et al. (2010); Umetsu et al. (2014, 2016); Pedersen & Dahle (2007); Shan et al. (2012); Applegate et al. (2014); Okabe & Smith (2016), for a total of 25 previous mass estimates. For clusters with multiple analyses, we considered the results reported in LC²-single.

We compared spherical WL masses within 1.0 Mpc (see Fig. 10) and within r_{200} (see Fig. 11). The agreement with previous results is good, $\ln M_{\mathrm{LC2}}/M_{\mathrm{PSZ2LenS}} \sim 0.10 \pm 0.38$ for masses within 1 Mpc

---

[5] The catalogues are available at http://pico.oabo.inaf.it/~sereno/CoMaLit/LC2/.

Table 3. WL mass measurements. Overdensity masses and radii are reported at $\Delta = 2500, 500, 200$, and at the viral overdensity Δ_{vir}, computed according to Bryan & Norman (1998). Spherical masses within fixed physical radii are reported within 0.5, 1.0 and 1.5 Mpc (columns 10, 11 and 12). M_Δ is the mass within the sphere of radius r_Δ. $M_{n\text{Mpc}}$ is the mass within the sphere of radius nMpc. Quoted values are the bi-weight estimators of the posterior probability distributions. Masses and radii are in units of 10^{14} M$_\odot$ and Mpc, respectively.

Index	M_{2500}	r_{2500}	M_{500}	r_{500}	M_{200}	r_{200}	M_{vir}	r_{vir}	$M_{0.5\text{Mpc}}$	$M_{1\text{Mpc}}$	$M_{1.5\text{Mpc}}$
21	3.2 ± 1.1	0.6 ± 0.1	7.2 ± 3.0	1.3 ± 0.2	10.0 ± 4.8	2.0 ± 0.3	12.1 ± 6.2	2.6 ± 0.5	2.6 ± 0.6	5.5 ± 1.5	7.9 ± 2.5
38	0.5 ± 0.4	0.3 ± 0.1	0.9 ± 0.7	0.7 ± 0.2	1.2 ± 0.9	1.0 ± 0.3	1.4 ± 1.1	1.3 ± 0.4	0.7 ± 0.4	1.2 ± 0.7	1.5 ± 1.0
43	1.6 ± 0.7	0.5 ± 0.1	3.1 ± 1.4	1.0 ± 0.2	4.1 ± 2.1	1.5 ± 0.3	4.8 ± 2.6	2.0 ± 0.4	1.7 ± 0.5	3.1 ± 1.0	4.0 ± 1.6
212	4.7 ± 1.2	0.6 ± 0.1	14.8 ± 4.0	1.5 ± 0.1	23.5 ± 7.8	2.4 ± 0.3	28.4 ± 10.2	3.0 ± 0.4	3.5 ± 0.5	8.9 ± 1.2	14.3 ± 2.4
215	0.7 ± 0.6	0.3 ± 0.1	1.3 ± 1.2	0.7 ± 0.2	1.7 ± 1.6	1.1 ± 0.4	2.0 ± 1.9	1.4 ± 0.5	0.9 ± 0.6	1.6 ± 1.2	2.1 ± 1.7
216	0.8 ± 0.7	0.3 ± 0.1	1.8 ± 1.7	0.8 ± 0.3	2.5 ± 2.4	1.2 ± 0.4	2.8 ± 2.9	1.5 ± 0.5	1.2 ± 0.7	2.2 ± 1.5	2.9 ± 2.2
243	0.6 ± 0.6	0.3 ± 0.1	1.2 ± 1.2	0.6 ± 0.2	1.7 ± 1.7	1.0 ± 0.4	1.9 ± 1.9	1.2 ± 0.4	1.0 ± 0.7	1.7 ± 1.3	2.2 ± 1.9
251	4.0 ± 1.3	0.6 ± 0.1	6.6 ± 2.2	1.2 ± 0.1	8.1 ± 2.9	1.8 ± 0.2	8.9 ± 3.3	2.2 ± 0.3	3.4 ± 0.8	5.7 ± 1.5	7.4 ± 2.1
268	1.2 ± 0.7	0.4 ± 0.1	2.5 ± 1.5	0.9 ± 0.2	3.5 ± 2.3	1.4 ± 0.3	4.1 ± 2.9	1.8 ± 0.4	1.4 ± 0.5	2.7 ± 1.2	3.6 ± 1.8
271	2.0 ± 1.1	0.5 ± 0.1	3.8 ± 2.2	1.0 ± 0.2	4.9 ± 3.1	1.4 ± 0.3	5.4 ± 3.6	1.7 ± 0.4	2.2 ± 0.8	3.8 ± 1.7	5.0 ± 2.5
329	2.5 ± 1.2	0.5 ± 0.1	9.9 ± 5.2	1.4 ± 0.3	17.3 ± 10.4	2.3 ± 0.5	22.2 ± 14.1	2.9 ± 0.6	2.4 ± 0.6	6.4 ± 1.8	10.7 ± 3.6
360	2.3 ± 1.4	0.5 ± 0.1	4.6 ± 2.8	1.1 ± 0.2	6.1 ± 4.1	1.6 ± 0.4	6.9 ± 4.8	1.9 ± 0.5	2.3 ± 0.9	4.3 ± 1.9	5.9 ± 2.9
370	1.1 ± 0.8	0.4 ± 0.1	2.8 ± 2.4	0.9 ± 0.3	4.0 ± 3.9	1.4 ± 0.5	4.8 ± 5.0	1.9 ± 0.7	1.4 ± 0.6	2.9 ± 1.7	4.1 ± 2.9
391	2.6 ± 0.9	0.5 ± 0.1	11.6 ± 3.6	1.5 ± 0.2	21.4 ± 7.9	2.4 ± 0.3	27.6 ± 11.0	3.1 ± 0.4	2.5 ± 0.4	7.1 ± 1.1	12.1 ± 2.2
446	1.6 ± 0.6	0.5 ± 0.1	4.9 ± 1.4	1.1 ± 0.1	7.8 ± 2.6	1.8 ± 0.2	9.9 ± 3.6	2.4 ± 0.3	1.8 ± 0.3	4.2 ± 0.7	6.5 ± 1.3
464	2.1 ± 0.6	0.5 ± 0.1	6.4 ± 1.5	1.2 ± 0.1	10.1 ± 2.7	2.0 ± 0.2	12.8 ± 3.8	2.6 ± 0.4	2.1 ± 0.4	5.0 ± 0.7	7.7 ± 1.3
473	0.5 ± 0.3	0.3 ± 0.1	1.1 ± 0.6	0.7 ± 0.1	1.6 ± 1.0	1.1 ± 0.2	2.0 ± 1.3	1.4 ± 0.3	0.8 ± 0.3	1.5 ± 0.6	2.1 ± 1.0
478	2.8 ± 1.3	0.5 ± 0.1	6.7 ± 3.1	1.1 ± 0.2	9.6 ± 5.2	1.6 ± 0.3	10.7 ± 6.1	1.9 ± 0.4	3.1 ± 0.9	6.3 ± 1.9	9.0 ± 3.4
547	1.3 ± 0.7	0.4 ± 0.1	6.6 ± 3.4	1.3 ± 0.2	12.5 ± 7.0	2.2 ± 0.4	17.5 ± 10.1	3.0 ± 0.6	1.6 ± 0.4	4.7 ± 1.4	8.0 ± 2.6
554	2.6 ± 1.5	0.5 ± 0.1	6.6 ± 4.7	1.1 ± 0.3	9.6 ± 8.0	1.8 ± 0.5	11.1 ± 9.8	2.1 ± 0.6	2.6 ± 0.9	5.6 ± 2.4	8.3 ± 4.4
586	2.6 ± 1.4	0.5 ± 0.1	5.0 ± 3.3	1.0 ± 0.2	6.4 ± 4.8	1.5 ± 0.4	7.0 ± 5.4	1.7 ± 0.4	2.8 ± 1.0	5.0 ± 2.4	6.6 ± 3.7
618	2.0 ± 0.9	0.5 ± 0.1	9.2 ± 4.3	1.5 ± 0.2	17.3 ± 9.3	2.4 ± 0.4	24.5 ± 14.1	3.4 ± 0.7	1.9 ± 0.4	5.5 ± 1.3	9.5 ± 2.6
721	1.7 ± 1.4	0.4 ± 0.1	4.2 ± 4.3	0.9 ± 0.3	5.9 ± 6.9	1.4 ± 0.6	6.6 ± 8.0	1.7 ± 0.7	2.1 ± 1.1	4.4 ± 3.0	6.3 ± 5.0
724	4.4 ± 1.2	0.6 ± 0.1	13.3 ± 3.7	1.6 ± 0.1	20.8 ± 7.5	2.5 ± 0.3	26.1 ± 10.6	3.3 ± 0.4	3.1 ± 0.5	7.8 ± 1.1	12.4 ± 2.1
729	0.6 ± 0.5	0.3 ± 0.1	1.5 ± 1.7	0.8 ± 0.3	2.1 ± 2.8	1.2 ± 0.5	2.5 ± 3.5	1.5 ± 0.7	1.0 ± 0.6	2.0 ± 1.6	2.8 ± 2.8
735	1.2 ± 0.9	0.4 ± 0.1	2.6 ± 2.1	0.8 ± 0.2	3.5 ± 3.1	1.2 ± 0.4	3.9 ± 3.6	1.4 ± 0.5	1.6 ± 0.8	3.0 ± 1.9	4.1 ± 2.8
804	0.7 ± 0.4	0.4 ± 0.1	1.7 ± 0.7	0.8 ± 0.1	2.4 ± 1.2	1.2 ± 0.2	2.9 ± 1.5	1.6 ± 0.3	1.1 ± 0.3	2.0 ± 0.7	2.8 ± 1.1
822	1.4 ± 0.5	0.4 ± 0.1	3.4 ± 1.1	1.0 ± 0.1	4.8 ± 1.8	1.5 ± 0.2	5.8 ± 2.3	1.9 ± 0.3	1.7 ± 0.4	3.4 ± 0.8	4.7 ± 1.3
902	4.2 ± 1.4	0.6 ± 0.1	7.5 ± 3.2	1.2 ± 0.2	9.5 ± 4.5	1.8 ± 0.3	10.6 ± 5.2	2.2 ± 0.4	3.6 ± 0.8	6.5 ± 1.9	8.6 ± 3.0
955	1.9 ± 1.5	0.4 ± 0.1	3.7 ± 2.9	0.9 ± 0.3	4.9 ± 4.0	1.4 ± 0.4	5.5 ± 4.6	1.7 ± 0.5	2.1 ± 1.2	3.8 ± 2.3	5.1 ± 3.3
956	3.9 ± 2.2	0.6 ± 0.1	8.4 ± 5.5	1.3 ± 0.3	11.3 ± 8.6	2.0 ± 0.5	13.0 ± 10.6	2.5 ± 0.7	3.1 ± 1.1	6.4 ± 2.6	9.1 ± 4.3
961	0.8 ± 0.7	0.3 ± 0.1	2.4 ± 2.6	0.7 ± 0.3	3.8 ± 4.6	1.2 ± 0.5	4.3 ± 5.4	1.4 ± 0.6	1.4 ± 0.9	3.1 ± 2.3	4.6 ± 3.9
1046	3.4 ± 0.9	0.6 ± 0.0	6.5 ± 1.9	1.2 ± 0.1	8.5 ± 2.9	1.8 ± 0.2	9.6 ± 3.4	2.1 ± 0.3	3.0 ± 0.5	5.6 ± 1.2	7.6 ± 1.9
1057	2.4 ± 0.6	0.5 ± 0.0	6.6 ± 1.8	1.2 ± 0.1	9.8 ± 3.2	1.9 ± 0.2	12.0 ± 4.3	2.5 ± 0.3	2.3 ± 0.4	5.3 ± 0.9	7.9 ± 1.6
1212	1.6 ± 1.2	0.4 ± 0.1	3.7 ± 2.9	1.0 ± 0.3	5.2 ± 4.4	1.6 ± 0.5	6.1 ± 5.5	2.0 ± 0.6	1.7 ± 0.8	3.6 ± 1.9	5.0 ± 3.1

and ∼0.12 ± 0.67 for M_{200}. The scatter is significant and it is difficult to look for biases, if any.

Four clusters in our sample were investigated in Gruen et al. (2014). The analysis of Gruen et al. (2014) was based on the same CFHTLS images but it is independent from ours for methods and tools. They used different pipelines for the determination of galaxy shapes and photometric redshifts; they selected background galaxies based on photometric redshift and they did not exploit colour–colour procedures; they considered a fitting radial range fixed in angular aperture ($2 < \theta < 15'$) rather than a range based on a fixed physical length; they measured the shear signal in annuli equally spaced in linear space, which give more weight to the outer regions, rather than intervals equally spaced in logarithmic space; they modelled the lens either as a single NFW profile with a (scattered) mass–concentration relation in line with Duffy et al. (2008) or as a multiple component halo. Notwithstanding the very different approaches, the agreement between the two analyses is good (see Figs 10 and 11).

The most notable difference is in the mass estimate of PSZ2 G099.86+58.45 (478), when they found $M_{500} = 18.1^{+5.8}_{-5.3} \times 10^{14}$ M$_\odot$. Part of the difference, which is however not statistically significant, can be ascribed to the cluster redshift $z_{\text{lens}} = 0.69$

assumed in Gruen et al. (2014), which was estimated through the median photometric redshift of 32 visually selected cluster member galaxies and is higher than ours.

Sereno & Ettori (2017) estimated the WL calibrated masses $M_{\text{WLc, 500}}$ of the 926 *Planck* clusters identified through the Matched Multi-Filter method MMF3 with measured redshift[6]. Masses were estimated based on the spherically integrated Compton parameter Y_{500}. They used as a calibration sample the LC^2-single catalogue and estimated the cluster mass with a forecasting procedure which does not suffer from selection effects, Malmquist/Eddington biases and time or mass evolution.

WL calibrated masses are available for 29 clusters in the PSZ2LenS sample. The comparison of masses within r_{500} is shown in Fig. 12. The agreement is good, $\ln M_{\text{WLc}}/M_{\text{PSZ2LenS}} \sim -0.03 \pm 0.67$.

---

[6] The catalogue HFI_PCCS_SZ-MMF3_R2.08_MWLC.DAT of *Planck* masses is available at http://pico.oabo.inaf.it/~sereno/CoMaLit/forecast/.
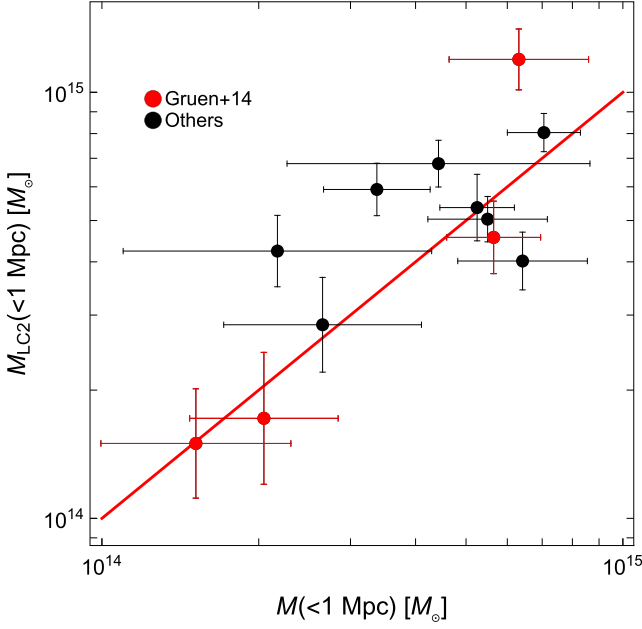
Figure 10. Comparison between the WL masses within 1 Mpc as measured in this analysis and the masses already available in literature through the LC2-single catalogue, M_{LC2}. Red points, as detailed in the legend, refer to the analysis in Gruen et al. (2014). The red full line indicates the perfect agreement.
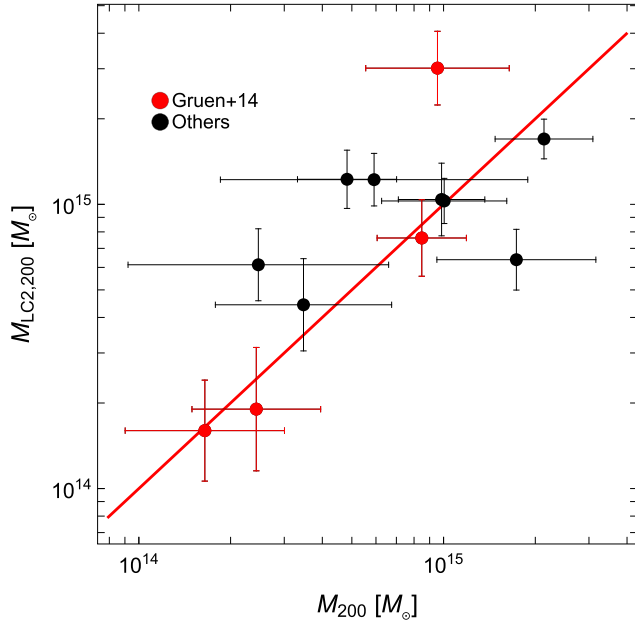

Figure 11. Comparison between the WL masses M_{200} as measured in this analysis and the masses $M_{LC2, 200}$ reported in the LC^2-single catalogue. Red points, as detailed in the legend, refer to the analysis in Gruen et al. (2014). The red full line indicates the perfect agreement.

10 CONCENTRATIONS

Masses and concentrations at the standard radius r_{200} are reported in Table 4. PSZ2LenS haloes are well fitted by cuspy models. The number of independent data usually outweighs the χ^2 value.

Due to the low SNR of the observations, concentrations can be tightly constrained only for a few massive haloes. The estimated concentrations can be strongly affected by the assumed priors.
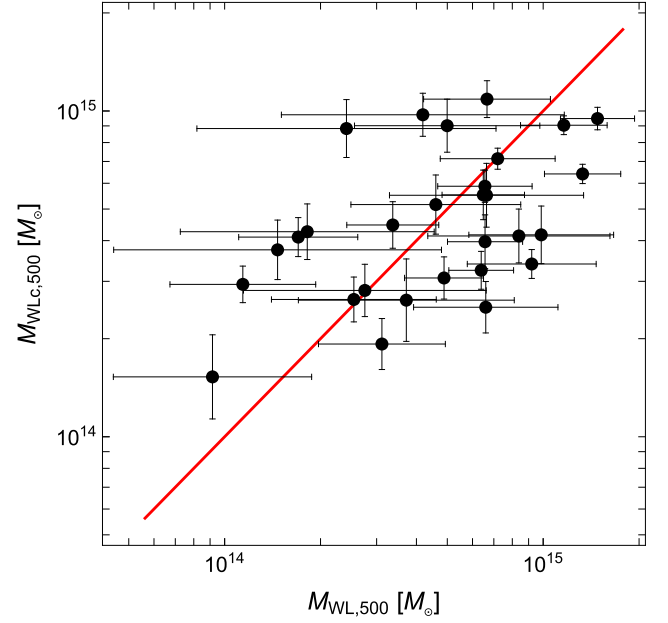

Figure 12. Comparison between the WL masses $M_{WL, 500}$, as measured in this analysis, and the masses $M_{WLc, 500}$, based on the Compton parameter Y_{500} and calibrated through a WL subsample by Sereno & Ettori (2017). The red full line indicates the perfect agreement.

Whereas the effect of the priors is negligible in massive clusters with high-quality observations (Umetsu et al. 2014; Sereno et al. 2015a), it can be significant when the SNR is lower (Sereno & Covone 2013; Sereno et al. 2015a). The prior which is uniform in logarithmic space rather than in linear space favours lower concentrations. There is no other way to circumvent this problem than deeper observations.

The value of the observed concentrations decreases with mass; see Fig. 13. As customary in analyses of the *c-M*, we modelled the relation with a power law,

$$c_{200} = 10^\alpha \left(\frac{1+z}{1+z_{\mathrm{ref}}} \right)^\gamma \left(\frac{M_{200}}{M_{\mathrm{pivot}}} \right)^\beta ; \qquad (21)$$

the intrinsic scatter $\sigma_{c|M}$ of the concentration around $c_{200}(M_{200})$ is taken to be lognormal (Duffy et al. 2008; Bhattacharya et al. 2013).

We performed a linear regression in decimal logarithmic (log) variables using the R-package LIRA[7]. LIRA performs a Bayesian hierarchical analysis which can deal with heteroscedastic and correlated measurements uncertainties, intrinsic scatter, scattered mass proxies and time-evolving mass distributions (Sereno 2016). In particular, the anti-correlation between the lensing measured mass and concentration makes the *c-M* relation apparently steeper (Auger et al. 2013; Du & Fan 2014; Dutton & Macciò 2014; Sereno et al. 2015a). When we correct for this, the observed relation is significantly flatter (Sereno et al. 2015a). On the other hand, neglecting the intrinsic scatter of the WL mass with respect to the true mass can bias the estimated slope towards flatter values (Rasia et al. 2012; Sereno & Ettori 2015b). We accounted for both uncertainty correlations and intrinsic scatter.

[7] The package LIRA (LInear Regression in Astronomy) is publicly available from the Comprehensive R Archive Network at https://cran.r-project.org/web/packages/lira/index.html. For further details, see Sereno (2016).

Table 4. Masses and concentrations. Column 1: cluster PSZ2 index; columns 2 and 3: bi-weight estimators of M_{200} and concentration c_{200}, respectively. Column 4: minimum χ^2. Column 5: number of radial annuli with background galaxies. Masses are in units of $10^{14}\,\mathrm{M_\odot}\,h^{-1}$.

Index	M_{200}	c_{200}	χ^2	N_{bins}
21	7.0 ± 3.3	5.4 ± 3.1	17.5	15
38	0.8 ± 0.6	9.3 ± 5.6	13.1	15
43	2.9 ± 1.5	8.8 ± 5.0	10.4	15
212	16.5 ± 5.5	2.9 ± 1.2	15.6	14
215	1.2 ± 1.1	8.6 ± 5.8	8.3	15
216	1.7 ± 1.7	7.5 ± 5.7	22.1	14
243	1.2 ± 1.2	8.1 ± 5.9	14.7	14
251	5.7 ± 2.0	12.8 ± 4.7	4.7	14
268	2.4 ± 1.6	7.5 ± 5.5	13.4	15
271	3.4 ± 2.2	9.6 ± 5.6	17.4	14
329	12.1 ± 7.3	2.0 ± 1.1	7.2	15
360	4.3 ± 2.9	8.2 ± 5.6	2.8	14
370	2.8 ± 2.8	5.0 ± 5.2	6.6	15
391	15.0 ± 5.5	1.8 ± 0.7	12.4	15
446	5.5 ± 1.8	2.9 ± 1.3	22.2	15
464	7.1 ± 1.9	2.9 ± 1.1	14.8	15
473	1.2 ± 0.7	5.1 ± 4.5	5.9	15
478	6.7 ± 3.6	5.4 ± 4.6	14.2	15
547	8.7 ± 4.9	1.6 ± 0.6	14.0	15
554	6.7 ± 5.6	5.1 ± 4.8	12.6	14
586	4.5 ± 3.4	8.9 ± 5.4	11.3	14
618	12.1 ± 6.5	1.6 ± 0.7	20.5	15
721	4.1 ± 4.8	4.8 ± 4.8	11.8	14
724	14.6 ± 5.2	3.2 ± 1.5	15.4	15
729	1.5 ± 2.0	4.0 ± 5.0	13.7	15
735	2.5 ± 2.2	7.6 ± 5.8	19.4	13
804	1.7 ± 0.8	5.5 ± 4.5	10.8	15
822	3.4 ± 1.3	4.7 ± 2.7	10.7	15
902	6.7 ± 3.2	9.6 ± 4.7	4.7	15
955	3.4 ± 2.8	9.0 ± 5.8	5.6	13
956	7.9 ± 6.1	7.3 ± 5.3	4.7	14
961	2.6 ± 3.2	3.3 ± 3.5	5.9	10
1046	5.9 ± 2.0	7.8 ± 3.8	26.0	15
1057	6.9 ± 2.3	3.7 ± 1.5	18.6	15
1212	3.6 ± 3.1	6.2 ± 5.4	5.2	14

A proper modelling of the mass distribution is critical to address Malmquist/Eddington biases (Kelly 2007). Within the LIRA scheme, the distribution of the covariate is modelled as a mixture of time-evolving Gaussian distributions, which can be smoothly truncated at low values to model skewness. The parameters of the distribution are found within the regression procedure. This scheme is fully effective in modelling both selection effects at low masses, where *Planck* candidates with SNR <4.5 are excluded, and the steepness of the cosmological halo mass function at large masses. We verified that this approach is appropriate for *Planck* selected objects in Sereno et al. (2015) and Sereno & Ettori (2015a). For the analysis of the mass–concentration relation of the PSZ2LenS sample, we modelled the mass distribution of the selected objects as a time-evolving Gaussian function.

We found $\alpha = 0.83 \pm 0.42$ (for $z_{ref} = 0.2$), $\beta = -0.27 \pm 0.57$, $\gamma = 0.77 \pm 0.88$. The relation between mass and concentration is in agreement with theoretical predictions (see Fig. 13), with a very marginal evidence for a slightly steeper relation. There is no evidence for a time evolution of the relation. The statistical uncertainties make it difficult to distinguish among competing theoretical predictions.
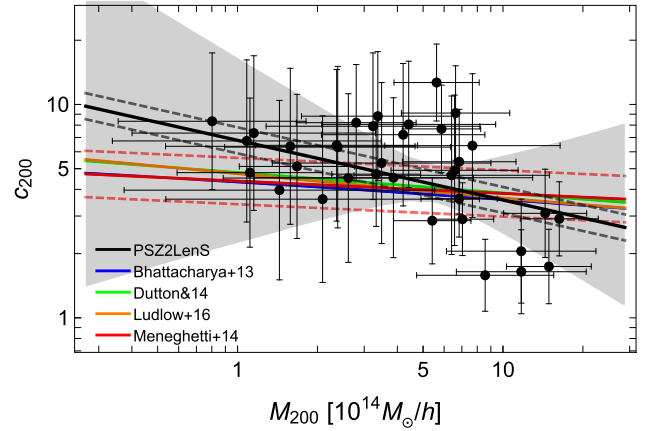

Figure 13. The mass–concentration relation of the PSZ2LenS clusters. The dashed black lines show the median scaling relation (full black line) plus or minus the intrinsic scatter at the median redshift $z = 0.20$. The shaded grey region encloses the 68.3 per cent confidence region around the median relation due to uncertainties on the scaling parameters. The blue, green, orange and red lines plot the mass–concentration relations of Bhattacharya et al. (2013), Dutton & Macciò (2014), Ludlow et al. (2016) and Meneghetti et al. (2014), respectively. The dashed red lines enclose the 1σ scatter region around Meneghetti et al. (2014).

The estimated scatter of the WL masses, $\sigma_{M_{WL}|M} = 0.11 \pm 0.08$, is in agreement with the analysis in Sereno & Ettori (2015b), whereas the scatter of the c–M relation, $\sigma_{c|M} = 0.06 \pm 0.05$, is in line with theoretical predictions (Bhattacharya et al. 2013; Meneghetti et al. 2014, $\sigma_{c|M} \sim 0.15$).

The observed relation between lensing mass and concentration can differ from the theoretical relation due to selection effects of the sample. Intrinsically overconcentrated clusters or haloes whose measured concentration is boosted due to their orientation along the line of sight may be overrepresented with respect to the global population in a sample of clusters selected according to their large Einstein radii or to the apparent X-ray morphology (Meneghetti et al. 2014; Sereno et al. 2015a).

The Bayesian method implemented in LIRA can correct for evolution effects in the sample, e.g. massive cluster preferentially included at high redshift (Sereno et al. 2015a). However, if the selected sample consists of a peculiar population of clusters which differ from the global population, we would measure the specific c–M relation of this peculiar sample.

Based on theoretical predictions, SZ–selected clusters should not be biased (see Section 1). We confirmed this view. We found no evidence for selection effects: the slope, the normalization, the time evolution and the scatter are in line with theoretical predictions based on statistically complete samples of massive clusters. However, the statistical uncertainties are large and we cannot read too much into it.

11 STACKING

The low signal-to-noise ratio hampers the analysis of single clusters. Some further considerations can be based on the stacked analysis. We followed the usual approach (Johnston et al. 2007; Mandelbaum et al. 2008; Oguri et al. 2012; Okabe et al. 2013; Covone et al. 2014): we first stacked the shear measurements of the PSZ2LenS clusters and we then fitted a single profile to the stacked signal.

We combined the lensing signal of multiple clusters in physical proper radii. This procedure does not bias the measurement of
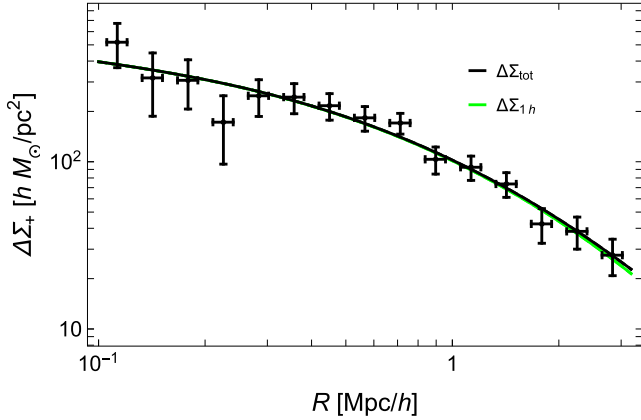
Figure 14. Stacked differential surface density $\Delta\Sigma_+$ of the PSZ2LenS clusters. Black points are our measurements. The vertical error bars show the square root of the diagonal values of the covariance matrix. The horizontal error bars are the weighted standard deviations of the distribution of radial distances in the annulus. The green curve plots the best-fitting contribution by the central halo; the black curve is the overall best-fitting radial profile including the 2-halo term.
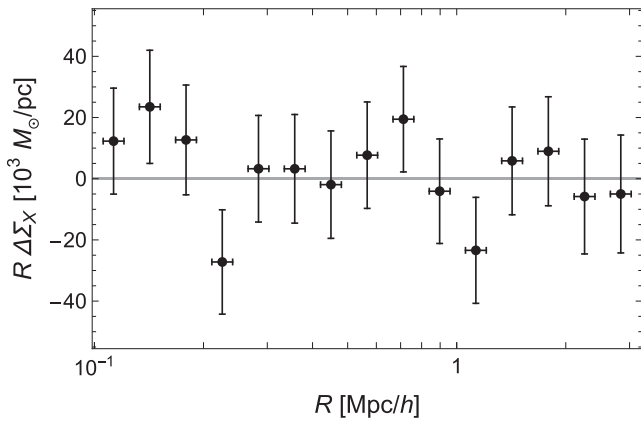

Figure 15. The renormalized cross-component of the differential shear profile of the stacked sample. Errors bars are as in Fig. 14.

mass and concentration since the weight factor is mass-independent for stacking in physical length units (Okabe et al. 2013; Umetsu et al. 2014). On the other hand, stacking in radial units after rescaling with the overdensity radius can bias the estimates of mass and concentration due to the mass-dependent weight factor (Okabe et al. 2013).

The standard approach we followed is effective in assessing the main properties of the sample. Alternatively, all shear profiles can be fitted at once assuming that all clusters share the same mass and concentration (Sereno & Covone 2013). More refined Bayesian hierarchical inference models have to be exploited to better study the population properties (Lieu et al. 2017).

The stacked signal is shown in Fig. 14. The detection level is of SNR = 14.3. As typical redshift of the stacked signal, we weighted the redshifts of the clusters by the lensing factor; see Appendix B. The effective lensing weighted redshift is $z_{stack} = 0.20$, which is consistent with the median redshift of the sample.

The cross-component of the shear profile, $\Delta\Sigma_\times$, is consistent with zero at all radii; see Fig. 15. This confirms that the main systematics are under control.

We analysed the stacked signal as a single lens; see Section 6. Since the cluster centres are well determined and we cut the inner 100 kpc h^{-1}, we did not model the fraction of miscentred haloes (Johnston et al. 2007; Sereno et al. 2015b), which we assumed to be null.

The stacked signal is well fitted by the truncated BMO halo plus the 2-halo term, $\chi^2 = 6.98$ for 15 bins; see Fig. 14. The contribution by the 2-halo is marginal even at large radii, i.e. $R \sim 3$ Mpc h^{-1}, the radial outer limit of the present analysis.

Mass, $M_{200} = (4.63 \pm 0.47) \times 10^{14}$ M$_\odot$ h^{-1}, and concentration, $c_{200} = 2.94 \pm 0.46$, of the stacked signal are in line with theoretical predictions; see Fig. 16.

The total stacked signal is mostly driven by very high SNR clusters at low redshifts. We then stacked the signal of the PSZ2LenS clusters in two redshifts bins below or above $z = 0.2$. The concentrations of both the low (see Fig. 16, middle panel) and high (see Fig. 16, bottom panel) redshift clusters are in line with theoretical predictions.

Recently, the CODEX (COnstrain Dark Energy with X-ray galaxy clusters) team performed a stacked WL analysis of 27 galaxy clusters at $0.40 \leq z \leq 0.62$ (Cibirka et al. 2017). The candidate CODEX clusters were selected in X-ray surface brightness and confirmed in optical richness. They found a stacked signal of $M_{200} \sim 6.6 \times 10^{14}$ M$_\odot$ h^{-1} and $c_{200} = 3.7$ at a median redshift of $z = 0.5$ in agreement with theoretical predictions.

The LoCuSS clusters were instead selected in X-ray luminosity. The analysis of the mass–concentration relation of the sample was found in agreement with numerical simulations and the stacked profile in agreement with the NFW profile (Okabe & Smith 2016).

Umetsu et al. (2016) analysed the stacked lensing signal of 16 X-ray regular CLASH clusters up to 4 Mpc h^{-1}. The profile was well fitted by cuspy dark-matter-dominated haloes in gravitational equilibrium, alike the NFW profile. They measured a mean concentration of $c_{200} \sim 3.8$ at $M_{200} \sim 9.9 \times 10^{14}$ M$_\odot$ h^{-1}.

Unlike previous samples, PSZ2Lens was SZ selected. Still, our results fit the same pattern and confirm ΛCDM predictions.

To check for systematics, we compared the stacked lensing mass to the composite halo mass profile $\langle M_{200}\rangle_{lw}$ from the sensitivity-weighted average of fits to individual cluster profiles (Umetsu et al. 2014, 2016); see Appendix B. From equation (B3) with $\Gamma = 0.65 \pm 0.10$, we obtain $\langle M_{200}\rangle_{lw} = (4.59 \pm 0.50) \times 10^{14}$ M$_\odot$ h^{-1}, in excellent agreement with the stacked mass, $M_{200} = (4.63 \pm 0.47) \times 10^{14}$ M$_\odot$ h^{-1}.

12 THE BIAS OF *Planck* MASSES

The bias of the *Planck* masses, i.e. the masses reported in the catalogues of the *Planck* collaboration, can be assessed by direct comparison with WL masses. For a detailed discussion of recent measurements of the bias, we refer to Sereno et al. (2015) and Sereno & Ettori (2017). Most of the previous studies had to identify counterparts of the PSZ2 clusters in previously selected samples of WL clusters. This can make the estimate of the bias strongly dependent on the calibration sample and on selection effects (Sereno & Ettori 2015b; Battaglia et al. 2016). In fact, WL calibration clusters usually sample the very high mass end of the halo mass function. If the mass comparison is limited to the subsample of SZ detected clusters with WL observations, the estimated bias cannot be representative of the full *Planck* sample.

Alternatively, *Planck* measurements can be viewed as follow-up observations of a pre-defined WL sample; see discussion in Battaglia et al. (2016). Non-detections can be accounted for by
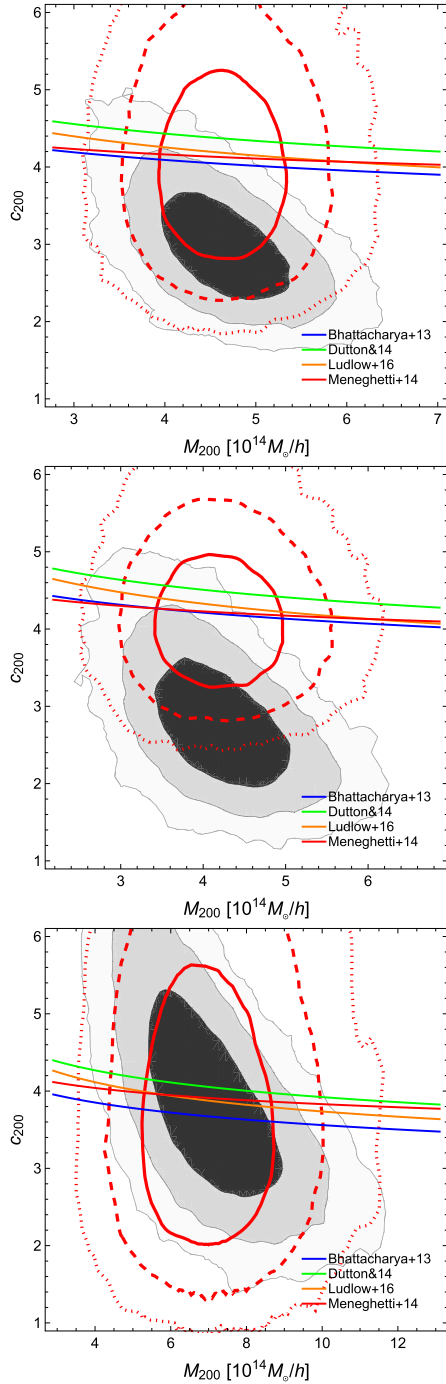
Figure 16. Marginalized probability distribution of mass and concentration of the stacked clusters. The grey shadowed regions include the 1σ, 2σ, 3σ confidence region in two dimensions, here defined as the regions within which the probability density is larger than $\exp[-2.3/2]$, $\exp[-6.17/2]$ and $\exp[-11.8/2]$ of the maximum, respectively. The blue, green, orange and red lines plot the mass–concentration relations of Bhattacharya et al. (2013), Dutton & Macciò (2014), Ludlow et al. (2016) and Meneghetti et al. (2014), respectively, at the effective redshift. The red contours trace the predicted concentration from Meneghetti et al. (2014), given the observed mass distribution and the predicted scatter of the theoretical mass–concentration relation. If needed, published relations were rescaled to our reference cosmology. Top panel. All clusters were stacked; the effective redshift is $z = 0.20$. Middle panel. Stacking of the clusters at $z_{\rm lens} < 0.2$; the effective redshift is $z = 0.14$. Bottom panel. Stacking of the clusters at $z_{\rm lens} > 0.2$; the effective redshift is $z = 0.33$.
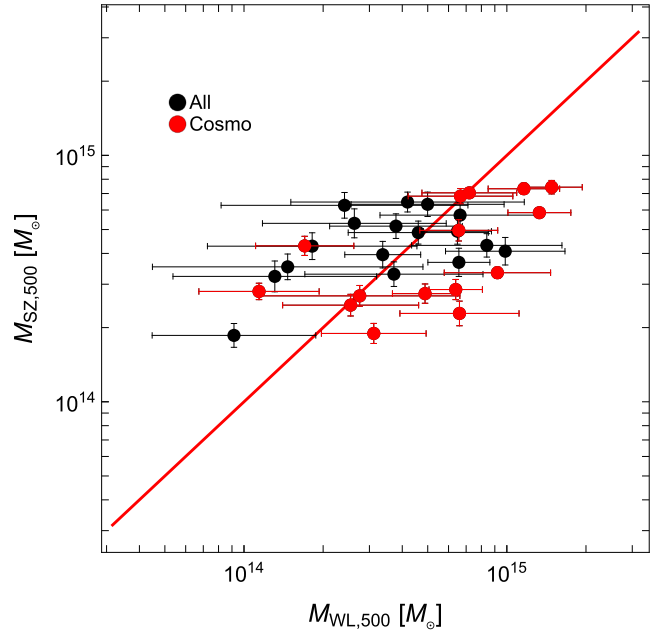
Figure 17. *Planck* SZ masses $M_{\rm SZ}$ versus WL masses $M_{\rm WL}$ for the PSZ2LenS clusters. Red dots mark the cosmological subsample. Masses are in units of $M_\odot$ and are computed within r_{500}. The red line shows the bisection $M_{\rm SZ} = M_{\rm WL}$.

setting the SZ signal of non-detected clusters to values corresponding to a multiple of the average noise in SZ measurements. As in the previous case, the calibration sample may be biased by selection effects with respect to the full PSZ2 sample. Here, the inclusion of non-detections makes the sample inconsistent with the *Planck* catalogue, which obviously includes only positive detections.

The estimate of the bias through the PSZ2LenS sample does not suffer from selection effects. It is a faithful and unbiased subsample of the whole population of *Planck* clusters. We can estimate the bias by comparing SZ to WL masses; see Fig. 17. To directly compare with the PSZ2 catalogue, we considered M_{500}.

We followed Sereno & Ettori (2017) and we estimated the bias $b_{\rm SZ}$ by fitting the relation[8]

$$\ln\langle M_{\rm SZ}\rangle = b_{\rm SZ} + \ln\langle M_{\rm WL}\rangle. \qquad (22)$$

We limited the analysis to the 32 clusters in PSZ2LenS, which had a published $M_{\rm SZ}$ mass in the *Planck* catalogues. We performed the regression with LIRA. We modelled the mass distribution of the selected objects as a Gaussian (Sereno & Ettori 2017). Corrections for Eddington/Malmquist biases were applied (Sereno & Ettori 2015b; Battaglia et al. 2016) and observational uncertainties and intrinsic scatters in WL and SZ masses were accounted for. We found $b_{\rm SZ} = -0.27 \pm 0.11$. The bias for the 15 clusters in the cosmological subsample is $b_{\rm SZ} = -0.40 \pm 0.14$, which is more prominent but still in good statistical agreement with the result for the full sample.

The intrinsic scatter of the WL masses is 23 ± 15 per cent, whereas the intrinsic scatter of the SZ masses is 12 ± 8 per cent. *Planck* masses are precise (thanks to the small scatter) but they are not accurate (due to the large bias).

---

[8] We define the bias as $b_{\rm SZ} = \ln M_{\rm SZ} - \ln M_{\rm WL}$. This definition slightly differs from that used in the *Planck* papers, where the bias is defined as $b_{\rm SZ} = M_{\rm SZ}/M_{500} - 1$. For low values of the bias, the difference is negligible.

Based on mock analyses, Shirasaki, Nagai & Lau (2016) found that enhanced scatter in relations confronting WL mass and thermal SZ effect originates from the combination of the projection of correlated structures along the line of sight and the uncertainty in the cluster radius associated with WL mass estimates. Here, we are considering M_{SZ} from the *Planck catalogue*, which were computed in an X-ray-based overdensity radius. This makes SZ and WL mass measurements uncorrelated but can increase the relation scatter (Sereno et al. 2015).

We determined the bias analysing the 32 clusters confirmed by both our inspection and the *Planck* team. Considering the candidates confirmed by *Planck* alone, we should include an additional candidate, PSZ2 G006.84+50.69 (PSZ2 index: 25), which is likely a substructure of the nearby larger PSZ2 G006.49+50.56 (21); see Section 14. Taking as lens position and redshift the PSZ2 catalogue entries, we can estimate a mass lens $M_{500} = (0.47 \pm 0.41) \times 10^{14}\, M_\odot$. The mass is compatible with a null signal (as expected since we did not find any suitable candidate counterpart) and would slightly reduce the size of the bias to $b_{SZ} = -0.24 \pm 0.11$.

Alternatively, we can assess the level of bias by comparing the effective WL mass $M_{WL, stack}$ of the stacked lensing profiles to the sensitivity-weighted average of the *Planck* masses $\langle M_{SZ}\rangle_{lw}$; see Appendix B. By assuming $\Gamma = 0.65 \pm 0.10$, we obtain $\ln(\langle M_{SZ}\rangle_{lw}/M_{WL, stack}) = -0.15 \pm 0.09$ in good agreement with our reference result.

Battaglia et al. (2016) argued that if the sample selection preserves the original *Planck* selection, as the case for PSZ2LenS, the factor b_{SZ} estimated through the *Planck* catalog masses can suffer by Eddington bias. By comparison with measurements by ACT, they estimated an Eddington bias correction of order of 15 per cent. In our reference result based on the linear regression, Eddington bias was accounted for by modelling the distribution of WL masses. The distribution of selected mass is quite symmetric. Assuming a log-normal distribution for the mass distribution, the Eddington bias turns out to be negligible when comparing mean values too (Sereno & Ettori 2017).

Our result is consistent with previous estimates based on WL comparisons. von der Linden et al. (2014b) found a large bias of $b_{SZ} = -0.30 \pm 0.06$ in the WtG sample (Applegate et al. 2014). Planck Collaboration et al. (2016c) measured $b_{SZ} = -0.32 \pm 0.07$ for the WtG sample, $b_{SZ} = -0.22 \pm 0.09$ for the CCCP (Hoekstra et al. 2015) sample and $b_{SZ} \sim 1$ from CMB lensing. The mean bias with respect to the LoCuSS sample is $b_{SZ} = -0.05 \pm 0.04$ (Smith et al. 2016).

The bias measurements reported in Table 5 for samples other than PSZ2LenS are taken from Sereno & Ettori (2017), which homogenized the estimates by adopting the same methodology we adopted here. Due to the different methods, the listed values can differ from the values quoted in the original analyses.

13 SYSTEMATICS

WL measurements of masses are very challenging. In fact, masses reported by distinct groups may differ by ~20–50 per cent (Applegate et al. 2014; Umetsu et al. 2014; Sereno & Ettori 2015b). Sources of systematics and residual statistical uncertainties may hinge on calibration errors, the fitting procedure, the selection of background galaxies and their photometric redshift measurements.

The presence of systematics may be tested by comparing results obtained with different methodologies and under different assumptions. Our results are consistent over a variegated sets of

Table 5. Bias of the *Planck* SZ masses with respect to WL masses. Values for calibration samples other than PSZ2LenS are taken from Sereno & Ettori (2017). Column 1: sample name. Column 2: number of WL clusters, N_{cl}. Columns 3 and 4: typical redshift and dispersion. Columns 5 and 6: typical WL mass and dispersion in units of $10^{14}\, M_\odot$. Column 7: mass bias $b_{SZ} = \ln(M_{SZ}/M_{WL})$. Typical values and dispersions are computed as bi-weighted estimators.

Sample	N_{Cl}	z	σ_z	M_{500}	$\sigma_{M_{500}}$	b_{SZ}
PSZ2LenS	32	0.20	0.15	4.8	3.4	-0.27 ± 0.11
PSZ2LenS Cosmo	15	0.13	0.09	6.4	4.1	-0.40 ± 0.14
LC²-single	135	0.24	0.14	7.8	4.8	-0.25 ± 0.04
CCCP	35	0.23	0.07	8.5	3.8	-0.22 ± 0.07
CLASH	13	0.37	0.13	11.3	3.3	-0.39 ± 0.08
LoCuSS	38	0.23	0.04	7.5	2.8	-0.18 ± 0.05
WtG	37	0.36	0.13	11.5	5.2	-0.43 ± 0.06

circumstances; see Tables 6 and 7. Systematic errors on the amplitude of the lensing signal $\Delta\Sigma_+$ are approximated as mass uncertainties through $M \sim \Delta\Sigma_+^{3/2}$; see Appendix B.

13.1 Background selection

The purity of the selected background galaxies is crucial to a proper WL analysis. Cluster members or foreground galaxies not properly identified can dilute the lensing signal. Contamination by foreground galaxies is most severe in the inner regions. We tried to overcome this by considering conservative selection criteria based on either photometric redshifts or colour–colour cuts. Our selection criteria suffer by a nominal $\gtrsim 1$ per cent contamination. The price for a conservative selection procedure is the low number of retained background galaxies.

13.1.1 Consistency

We checked for consistency by redoing the analysis and considering the selection procedures separately; see Table 6. The two selection criteria, i.e. cuts either in z_{phot} or in $g - r - i$ colours, are complementary. On average, only 15 per cent of the total number of retained galaxies are selected by both methods. The percentage is slightly higher (~18 per cent) for low redshift clusters ($z_{lens} < 0.2$).

The colour–colour cuts are very effective in selecting background galaxies at $z \gtrsim 0.7$, whereas the z_{phot} method can also sample lower redshifts sources. As a consequence, the effective source redshift of the galaxies selected by the $g - r - i$ cuts is larger. On one side, these galaxies have a large lensing depth due to the geometrical distance factor. On the other side, the z_{phot} method selects nearer and brighter galaxies, whose shape is better determined and which have a larger shear weight.

The comparison of the estimated differential surface density as obtained with the two different selection methods is shown in Fig. 18. Measurements are very well consistent within the statistical uncertainties.

We also re-estimated the masses adopting the reference fitting scheme for each selection method. Results are listed in Table 6. For clusters with high SNR, the agreement between the masses estimates is excellent. For lower SNR lenses, the statistical agreement is still good but the uncertainties affecting the mass estimates are very large and the comparison is not so significant. The complementarity and the consistent results justify the combined use of the two selection methods.

Table 6. WL analyses exploiting different methods for the selection of background galaxies. Column 1: cluster PSZ2 index. Column 2: cluster redshift. Column 3: raw number density of background lensing sources per square arc minute, including objects with measured shape. Sources were selected with either the colour cuts or the photometric redshift methods. Column 4: effective source redshift. Column 5: WL SNR. Column 6: M_{200} in units of $10^{14}\,\mathrm{M}_{\odot}\,h^{-1}$. Quoted values are the bi-weight estimators of the posterior probability distributions. Columns 7, 8, 9 and 10: same as columns 3, 4, 5 and 6 but for sources selected with the colour–colour cuts only. Columns 11, 12, 13 and 14: same as columns 3, 4, 5 and 6 but for sources selected with the photometric redshifts only.

| | | *gri* OR z_{phot} | | | *gri* | | | | z_{phot} | | | |
Index	z	n_g z_{back}	SNR	M_{200}	n_g	z_{back}	SNR	M_{200}	n_g	z_{back}	SNR	M_{200}
21	0.078	1.61 0.71	2.7	7.0 ± 3.3	1.02	0.91	3.4	14.1 ± 6.7	0.83	0.61	1.0	3.3 ± 2.5
38	0.044	3.02 0.75	–0.2	0.8 ± 0.6	1.99	0.93	0.5	1.2 ± 1.1	1.60	0.65	–0.7	1.2 ± 0.8
43	0.034	3.18 0.73	2.3	2.9 ± 1.5	2.02	0.92	2.8	4.8 ± 1.9	1.73	0.63	1.3	2.3 ± 1.7
212	0.327	3.71 0.88	5.7	16.5 ± 5.5	3.08	0.91	5.4	16.5 ± 7.0	1.49	0.79	4.5	16.9 ± 8.2
215	0.151	1.15 0.69	–0.3	1.2 ± 1.1	0.66	0.87	0.1	2.6 ± 2.3	0.71	0.62	–0.2	1.4 ± 1.4
216	0.234	1.40 0.82	0.1	1.7 ± 1.7	1.02	0.92	–0.6	2.9 ± 2.1	0.63	0.72	0.9	3.3 ± 4.1
243	0.400	1.59 0.91	0.1	1.2 ± 1.2	1.38	0.92	0.0	1.9 ± 1.6	0.46	0.84	0.8	2.1 ± 2.3
251	0.222	2.54 0.85	1.9	5.7 ± 2.0	1.96	0.93	1.5	5.5 ± 2.3	1.01	0.73	1.1	5.4 ± 3.0
268	0.082	2.99 0.67	1.8	2.4 ± 1.6	1.70	0.90	0.9	2.0 ± 1.5	1.75	0.59	1.6	2.5 ± 2.1
271	0.336	2.26 0.89	1.7	3.4 ± 2.2	1.80	0.93	1.2	2.5 ± 2.1	0.86	0.81	1.8	9.3 ± 7.4
329	0.251	1.56 0.86	3.0	12.1 ± 7.3	0.79	1.24	1.0	3.2 ± 5.2	0.84	0.74	3.0	15.9 ± 8.8
360	0.279	2.04 0.80	1.2	4.3 ± 2.9	1.52	0.86	0.7	5.0 ± 3.7	0.95	0.74	1.0	5.8 ± 4.3
370	0.140	1.45 0.69	1.4	2.8 ± 2.8	0.86	0.86	2.5	17.6 ± 12.4	0.87	0.63	1.0	3.4 ± 3.4
391	0.277	4.21 0.87	5.3	15.0 ± 5.5	3.37	0.93	5.1	16.0 ± 4.5	1.70	0.78	2.9	10.6 ± 6.6
446	0.140	8.53 0.77	4.5	5.5 ± 1.8	6.12	0.91	3.6	5.0 ± 2.1	5.44	0.70	3.5	5.7 ± 2.0
464	0.141	9.55 0.75	5.5	7.1 ± 1.9	6.51	0.91	4.5	7.6 ± 2.1	6.38	0.69	4.9	6.9 ± 2.2
473	0.106	11.24 0.76	2.3	1.2 ± 0.7	8.11	0.90	1.8	1.1 ± 0.7	7.42	0.70	2.5	1.7 ± 0.9
478	0.630	7.43 0.97	2.9	6.7 ± 3.6	7.00	0.96	3.1	7.6 ± 3.9	1.65	1.03	2.6	15.1 ± 10.2
547	0.081	2.38 0.69	2.9	8.7 ± 4.9	0.96	1.03	1.1	4.7 ± 4.4	1.60	0.62	2.8	10.1 ± 5.6
554	0.384	2.01 0.91	2.4	6.7 ± 5.6	1.18	1.03	1.1	5.5 ± 3.7	1.04	0.83	2.0	8.3 ± 7.1
586	0.545	1.09 1.16	0.5	4.5 ± 3.4	0.80	1.25	1.0	6.9 ± 5.3	0.34	1.01	–0.9	4.5 ± 4.4
618	0.045	1.87 0.68	4.2	12.1 ± 6.5	0.84	0.98	1.2	2.8 ± 3.5	1.23	0.61	4.1	13.7 ± 7.9
721	0.528	1.51 0.88	0.9	4.1 ± 4.8	1.36	0.88	0.5	4.1 ± 4.8	0.31	0.91	0.2	7.9 ± 10.4
724	0.135	3.66 0.75	6.5	14.6 ± 5.2	2.40	0.90	5.9	26.2 ± 8.0	1.89	0.65	4.6	12.9 ± 4.9
729	0.199	2.14 0.79	1.4	1.5 ± 2.0	1.46	0.90	0.9	1.3 ± 1.7	1.03	0.70	1.4	2.9 ± 4.3
735	0.470	2.45 0.92	1.0	2.5 ± 2.2	2.23	0.92	1.4	3.0 ± 2.6	0.59	0.89	0.4	5.1 ± 4.8
804	0.140	14.01 0.76	2.6	1.7 ± 0.8	9.31	0.95	2.2	2.2 ± 1.0	12.81	0.76	2.3	1.6 ± 0.8
822	0.185	10.80 0.79	3.1	3.4 ± 1.3	7.04	0.99	1.9	2.2 ± 1.1	9.96	0.79	3.5	4.1 ± 1.5
902	0.350	2.35 0.90	1.3	6.7 ± 3.2	1.95	0.91	1.1	6.3 ± 3.2	0.78	0.85	2.4	14.8 ± 7.7
955	0.400	1.30 1.04	-0.1	3.4 ± 2.8	0.92	1.27	0.1	3.6 ± 3.1	0.43	0.83	–0.1	5.9 ± 5.5
956	0.188	0.90 0.69	1.7	7.9 ± 6.1	0.25	1.19	1.3	15.6 ± 6.5	0.68	0.64	1.3	7.9 ± 8.1
961	0.600	0.31 1.16	0.3	2.6 ± 3.2	0.21	1.23	0.2	1.1 ± 1.1	0.11	1.04	0.4	41.2 ± 27.1
1046	0.294	5.13 0.86	2.2	5.9 ± 2.0	4.32	0.91	2.6	8.0 ± 2.8	2.92	0.78	1.6	5.2 ± 2.1
1057	0.192	4.71 0.78	5.1	6.9 ± 2.3	3.22	0.90	4.2	6.9 ± 2.4	3.01	0.71	4.1	6.0 ± 3.0
1212	0.154	1.20 0.72	0.9	3.6 ± 3.1	0.43	1.30	1.8	16.1 ± 13.4	0.82	0.64	0.1	2.5 ± 2.2
Stack	0.203	127.29 0.79	14.3	4.63 ± 0.47	89.81	0.93	12.0	4.78 ± 0.56	75.86	0.71	11.6	4.59 ± 0.57

13.1.2 Cluster member dilution

Cluster members can dilute the lensing signal mostly in central regions. Thanks to our conservative background selection, this effect is not significant in our analysis and we preferred not to introduce corrective boosting factors. We checked the dilution effects in two ways. First, the radial distribution of the number density profile is constant to a good degree, with no bump in the inner regions (see Fig. 19).

Secondly, the mass measurement does not change significantly if we excise a larger inner region; see columns 2 and 4 of Table 7. In particular, if we set $R_{\mathrm{min}} = 0.5\,\mathrm{Mpc}\,h^{-1}$, the estimated mass M_{200} of the stacked profile changes by ∼6 per cent, well below the uncertainty of ∼10 per cent. The variation is due to the lower statistical power of the data sets (excluding the inner bins, the SNR is 12.1) and the lower capability of breaking the mass–concentration degeneracy rather than being significant of a systematic uncertainty.

13.1.3 Foreground contamination

In Section 5, we showed that the contamination affecting the sample of selected background galaxies is contained to the $\lesssim 2$ per cent level. Since in absence of intrinsic alignments foreground galaxies do not contribute a net shear signal, the contamination depletes the shear signal by the same amount, which causes an underestimation of the mass by $\lesssim 3$ per cent.

13.2 Priors

The effect of priors on mass and concentration is usually negligible but it can play a role when the SNR of the observations is low. Regression results obtained under different assumptions are summarized in Table 7.

Differences among prior schemes are smaller than statistical uncertainties. The only scheme which gives systematically lower masses, mostly at the low mass tail, is that exploiting priors which

Table 7. Masses determined assuming different halo modellings, priors or radial ranges. The setting is specified in the first five rows before the line break, where we list the density profile of the main halo (either NFW or BMO in row 1), the priors for mass (row 2), concentration (row 3) and halo bias (row 4), and the radial range (row 5). The symbols $\mathcal{U}$, $\log\mathcal{U}$, $\log\mathcal{N}$ and δ denote the uniform prior in linear space, the uniform prior in log-intervals, the lognormal distribution, and the Dirac delta, respectively. Mass priors are renormalized between 0.05 and $100 \times 10^{14}\,\mathrm{M}_\odot\,h^{-1}$, concentration priors between $c_{200} = 1$ and 20. For the halo bias, the function $b_\mathrm{h}[\nu(M_{200}, z)]$ follows Tinker et al. (2010). For the reference case (column 2), we also report the best-fitting value in round brackets. Cluster PSZ2 indexes are listed in Column 1. Masses are in units of $10^{14}\,\mathrm{M}_\odot\,h^{-1}$, lengths in units of $\mathrm{Mpc}\,h^{-1}$. Bi-weight estimators of central location and scale of the posterior distributions are reported.

1-halo	BMO	BMO	BMO	BMO	NFW	NFW	NFW
$p_\mathrm{prior}(M_{200})$	$\mathcal{U}$	$\mathcal{U}$	$\mathcal{U}$	$\log\mathcal{U}$	$\mathcal{U}$	$\mathcal{U}$	$\mathcal{U}$
$p_\mathrm{prior}(c_{200})$	$\mathcal{U}$	$\log\mathcal{N}$	$\mathcal{U}$	$\log\mathcal{U}$	$\mathcal{U}$	$\log\mathcal{N}$	$\mathcal{U}$
$p_\mathrm{prior}(b_\mathrm{h})$	$\delta[b_\mathrm{h}(\nu)]$	$\delta[b_\mathrm{h}(\nu)]$	$\delta[b_\mathrm{h}(\nu)]$	$\delta[b_\mathrm{h}(\nu)]$	$\delta[0]$	$\delta[0]$	$\delta[0]$
R-range	[0.1, 3]	[0.1, 3]	[0.5, 3]	[0.1, 3]	[0.1, 3]	[0.1, 3]	[0.1, 2]
21	7.0(7.8) ± 3.3	9.1 ± 3.7	9.1 ± 2.7	6.3 ± 3.4	6.7 ± 3.2	8.5 ± 3.5	9.4 ± 6.0
38	0.8(0.5) ± 0.6	1.1 ± 0.9	1.3 ± 0.9	0.4 ± 0.4	0.8 ± 0.6	0.9 ± 0.7	1.2 ± 0.9
43	2.9(2.8) ± 1.5	3.7 ± 1.7	2.8 ± 1.8	2.5 ± 1.5	2.8 ± 1.5	3.7 ± 1.9	2.5 ± 1.3
212	16.5(16.3) ± 5.5	14.4 ± 4.4	12.8 ± 5.1	15.1 ± 5.0	16.3 ± 5.7	16.7 ± 5.7	12.2 ± 4.6
215	1.2(0.2) ± 1.1	1.6 ± 1.7	2.6 ± 2.0	0.3 ± 0.4	1.5 ± 1.6	1.7 ± 2.1	1.4 ± 1.6
216	1.7(0.6) ± 1.7	2.5 ± 2.4	3.6 ± 3.2	0.6 ± 0.9	1.7 ± 1.6	2.2 ± 2.0	1.7 ± 1.7
243	1.2(0.1) ± 1.2	1.7 ± 1.8	1.4 ± 1.4	0.3 ± 0.3	1.2 ± 1.2	1.5 ± 1.6	0.9 ± 0.9
251	5.7(4.8) ± 2.0	6.4 ± 2.4	5.1 ± 2.5	5.6 ± 2.1	5.6 ± 1.8	7.1 ± 2.8	6.2 ± 2.2
268	2.4(2.9) ± 1.6	3.5 ± 2.1	4.1 ± 2.0	1.7 ± 1.6	2.2 ± 1.4	2.9 ± 1.8	2.1 ± 1.5
271	3.4(2.1) ± 2.2	5.3 ± 3.0	4.1 ± 2.6	2.0 ± 1.8	4.2 ± 3.1	5.0 ± 2.7	2.7 ± 1.6
329	12.1(15.4) ± 7.3	15.7 ± 7.5	11.3 ± 4.1	8.8 ± 6.1	9.6 ± 5.1	12.2 ± 5.8	9.9 ± 5.2
360	4.3(4.5) ± 2.9	5.6 ± 3.4	4.9 ± 3.0	2.5 ± 2.5	4.6 ± 3.0	5.6 ± 3.4	5.8 ± 4.4
370	2.8(4.1) ± 2.8	4.3 ± 3.3	3.5 ± 2.7	1.1 ± 1.6	2.7 ± 2.4	5.8 ± 4.8	2.6 ± 2.7
391	15.0(17.8) ± 5.5	14.8 ± 5.5	15.1 ± 5.5	14.3 ± 4.8	13.0 ± 4.9	13.9 ± 4.9	9.1 ± 4.3
446	5.5(5.6) ± 1.8	5.6 ± 1.7	5.7 ± 1.5	5.5 ± 2.0	5.2 ± 1.8	5.0 ± 1.7	5.1 ± 2.2
464	7.1(7.2) ± 1.9	7.1 ± 1.7	6.3 ± 1.4	6.9 ± 1.8	6.5 ± 1.7	6.5 ± 1.6	8.5 ± 2.7
473	1.2(1.5) ± 0.7	1.5 ± 0.8	1.5 ± 0.7	1.0 ± 0.7	1.1 ± 0.6	1.4 ± 0.7	1.0 ± 0.6
478	6.7(9.0) ± 3.6	8.6 ± 3.5	7.4 ± 2.9	5.9 ± 3.8	7.2 ± 3.7	7.8 ± 3.5	8.3 ± 7.2
547	8.7(9.3) ± 4.9	8.2 ± 4.8	8.1 ± 3.6	6.4 ± 4.6	7.2 ± 4.8	8.1 ± 4.5	4.8 ± 4.8
554	6.7(13.2) ± 5.6	7.7 ± 4.5	9.8 ± 6.0	4.2 ± 4.8	7.0 ± 4.9	9.7 ± 6.3	4.1 ± 3.4
586	4.5(2.5) ± 3.4	6.8 ± 4.8	5.7 ± 4.9	2.2 ± 2.8	4.0 ± 3.6	6.4 ± 3.6	5.6 ± 5.0
618	12.1(15.7) ± 6.5	10.3 ± 5.0	7.5 ± 4.7	10.3 ± 6.2	9.9 ± 6.4	10.1 ± 5.3	3.1 ± 2.5
721	4.1(3.7) ± 4.8	6.1 ± 5.3	7.1 ± 6.0	0.5 ± 0.7	7.0 ± 7.3	6.3 ± 5.3	2.6 ± 3.0
724	14.6(14.4) ± 5.2	15.7 ± 4.8	15.5 ± 5.2	12.7 ± 3.9	14.3 ± 4.6	15.4 ± 4.3	8.7 ± 3.9
729	1.5(2.5) ± 2.0	2.1 ± 2.1	3.1 ± 2.8	0.3 ± 0.4	1.9 ± 2.5	2.2 ± 2.1	0.8 ± 0.9
735	2.5(2.8) ± 2.2	3.3 ± 3.1	4.3 ± 3.0	0.7 ± 1.1	2.4 ± 2.2	3.0 ± 2.1	2.3 ± 2.1
804	1.7(2.0) ± 0.8	2.0 ± 0.9	1.8 ± 0.8	1.5 ± 0.9	1.6 ± 0.7	1.8 ± 0.8	2.0 ± 1.0
822	3.4(3.7) ± 1.3	3.9 ± 1.5	3.6 ± 1.2	3.2 ± 1.3	3.1 ± 1.2	3.5 ± 1.2	3.6 ± 1.6
902	6.7(6.6) ± 3.2	9.1 ± 4.4	6.0 ± 3.4	6.0 ± 2.6	6.2 ± 2.9	8.4 ± 3.2	8.0 ± 4.6
955	3.4(1.8) ± 2.8	5.4 ± 5.1	4.2 ± 3.8	0.5 ± 0.9	3.3 ± 2.6	5.4 ± 5.2	4.0 ± 3.0
956	7.9(7.6) ± 6.1	9.9 ± 6.4	8.2 ± 6.0	3.0 ± 2.9	6.4 ± 5.4	9.5 ± 7.1	6.2 ± 4.1
961	2.6(0.1) ± 3.2	6.9 ± 6.8	16.5 ± 17.1	0.3 ± 0.5	2.9 ± 4.2	4.5 ± 4.2	1.5 ± 1.7
1046	5.9(6.3) ± 2.0	7.4 ± 2.3	6.3 ± 2.0	5.7 ± 2.0	5.8 ± 2.0	6.8 ± 2.2	11.8 ± 4.7
1057	6.9(7.0) ± 2.3	7.7 ± 2.5	5.4 ± 1.5	6.6 ± 2.2	6.7 ± 2.3	7.0 ± 2.0	6.1 ± 2.2
1212	3.6(3.8) ± 3.1	5.6 ± 4.8	5.8 ± 3.2	1.4 ± 1.9	3.4 ± 2.6	4.1 ± 3.0	4.0 ± 3.7
Stack	4.63(4.65) ± 0.47	4.65 ± 0.45	4.34 ± 0.47	4.64 ± 0.46	4.35 ± 0.43	4.33 ± 0.42	4.43 ± 0.56

are uniform in logarithmic units; see column 5 of Table 7. For low SNR systems, these priors can bias the results towards lower values. This has to be counterbalanced by a careful choice of the lower mass limit, which can make the prior informative again. For this reason, we preferred uniform priors in linear space.

We verified that a more informative prior on the concentration inspired by numerical simulations (see columns 3 and 7 of Table 7) significantly improves neither the accuracy nor the precision; compare with columns 2 and 6 of Table 7, which makes the less informative priors preferable.

13.3 Mass estimator

A careful choice of the estimator is crucial. The choice has to be tuned to the quality of the data (Beers et al. 1990). In particular, the maximum likelihood method can be less stable in low SNR systems; see Appendix C. At the low mass end, the best-fitting value can underestimate the mass with respect to the bi-weight estimator; see column 2 of Table 7. However, differences are smaller than the statistical uncertainties. For larger mass clusters, differences are negligible.

13.4 Halo modelling

Recent *N*-body simulations have shown that the traditional NFW functional form may fail to describe the structural properties of cosmic objects at the percent level required by precision cosmology (Dutton & Macciò 2014; Meneghetti et al. 2014; Klypin et al. 2016).

The Einasto radial profiles can provide a more accurate description of the main halo. Sereno et al. (2016) computed the systematic errors expected for WL analyses of clusters of galaxies if one wrongly models the lens density profile. At the typical mass of
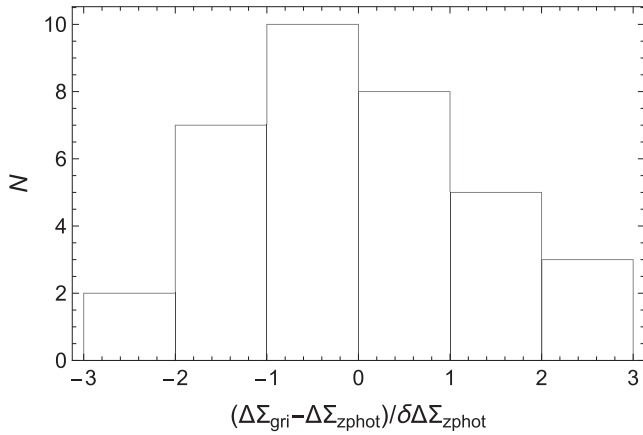
Figure 18. Distribution of the differences between the differential surface density as measured with a background source population of galaxies selected with the photometric redshifts, $\Delta\Sigma_{zphot}$, or with the $g - r - i$ colour–colour method, $\Delta\Sigma_{gri}$. The difference is in units of the statistical uncertainties on $\Delta\Sigma_{zphot}$. We plotted the shear signals generated by the PSZ2LenS clusters in the outer annulus, $2.51 \leq R \leq 3.16\,\mathrm{Mpc}\,h^{-1}$.
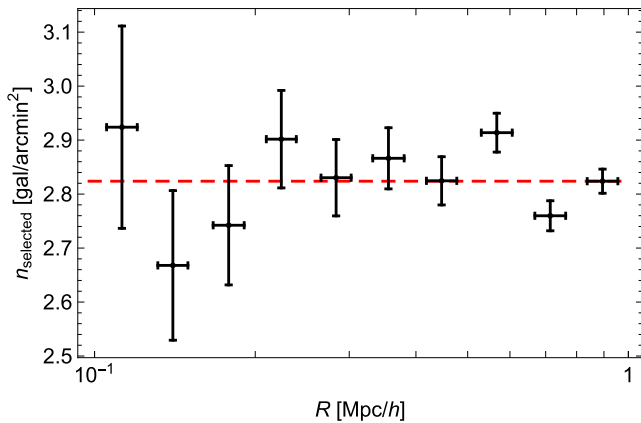

Figure 19. Mean number density profile of the selected background sources as a function of the radial distance from the cluster centre.

the PSZ2LenS clusters, $M_{200} \sim 4.6 \times 10^{14}\,\mathrm{M_\odot}\,h^{-1}$, the systematic error is below the per cent level whereas the viral masses and concentrations of the most massive haloes at $M_{200} \sim 10^{15}\,\mathrm{M_\odot}\,h^{-1}$ can be over- and underestimated by ∼5 per cent, respectively.

The inclusion of the inner regions, $R_{min} = 0.1\,\mathrm{Mpc}\,h^{-1}$ in column 2 of Table 7, does not significantly improve the statistical accuracy of the results with respect to fitting procedure neglecting them, $R_{min} = 0.5\,\mathrm{Mpc}\,h^{-1}$ in column 4, but it can make the results more accurate, thanks to a much better determination of the concentration and the breaking of the related degeneracy.

The proper modelling of the outer parts of the shear profile can be crucial in high SNR systems. For analyses that include the outer regions, i.e. $R \gtrsim 2\,\mathrm{Mpc}\,h^{-1}$, the effect of correlated matter may be significant and the use of the NFW profile can be worrisome (Oguri & Hamana 2011). The truncation of the profile can remove the unphysical divergence of the total mass of the NFW halo and partially removes systematic errors. However, only accounting for the 2-halo term can accurately describe the transition between the cluster and the correlated matter which occurs beyond the virial radius in the transition region from the infalling to the collapsed material (Diemer & Kravtsov 2014).

Thanks to our treatment of the 2-halo term, we could fit the shear profile up to large radii, $R = 3.16\,\mathrm{Mpc}\,h^{-1}$. Even though differences are smaller than statistical uncertainties, some features emerge. The inclusion of the outer regions improves both accuracy, i.e. the size of the systematic error, and precision, i.e. the size of the statistical uncertainty.

If we do not truncate the main halo and we do not consider the 2-halo term, fitting up to large radii can underestimate the halo concentration and bias the mass high (Oguri & Hamana 2011). We found that the NFW fitting out to large radii (see column 6 of of Table 7) can overestimate masses with respect to the more complete modelling based on the truncated BMO density profile plus the 2-halo term (see column 2 of Table 7). By proper modelling the outer regions, we correct a potential systematic error of ∼6 per cent.

Inclusion of outer regions can significantly improve the precision too. As can be seen from the comparison of the case in column 6 of Table 7, where $R_{min} = 3.16\,\mathrm{Mpc}\,h^{-1}$ with the case $R_{min} = 2.0\,\mathrm{Mpc}\,h^{-1}$ in column 8, the statistical uncertainty decreases by ∼25 per cent. This feature is crucial in low SNR systems where most of the signal is collected in the outer regions.

In summary, residual systematic bias due to halo modelling is at the per cent level if we properly model the deviations from the NFW profile, mostly at large radii.

13.5 Centring

Locating the centres of dark matter haloes is critical for the unbiased analysis of mass profiles (George et al. 2012). Miscentring leads to underestimate $\Delta\Sigma_+$ at small scales and to bias low the measurement of the concentration (Johnston et al. 2007).

We identified the centre of the cluster as the BCG. Bright galaxies or X-ray emission from hot plasma can be used to trace the halo centre. George et al. (2012) investigated the consequences of miscentring on the WL signal from a sample of 129 X-ray-selected galaxy groups in the COSMOS field with redshifts $0 \lesssim z \lesssim 1$ and halo masses in the range 10^{13}–$10^{14}\,\mathrm{M_\odot}$. By measuring the stacked lensing signal around different candidate centres, they found that massive galaxies near the X-ray centroids trace the centre of mass to $\lesssim 75\,\mathrm{kpc}$, whereas the X-ray position or the centroids based on the mean position of member galaxies have larger offsets primarily due to the statistical uncertainties in their positions (typically ∼50–150kpc).

In complex clusters, the BCG defining the cluster centre might be misidentified or it might not coincide with the matter centroid, but this second effect is generally small and negligible at the WL scale (George et al. 2012; Zitrin et al. 2012).

Our choice to identify the BCG as the cluster centre and to cut the inner $R < 0.1\,\mathrm{Mpc}\,h^{-1}$ region makes the effects of miscentring of second order in our analysis. We checked this by re-extracting the shear signal of the clusters around the SZ centroid and by re-computing the masses as described in Section 8. Masses are consistent and differences are well below the statistical uncertainties (see Fig. 20 and Table 8). By comparing the stacked profiles, we found that the systematic error in mass due to off-centring is negligible (∼0.5 per cent).

In fact, the typical displacement between the BCG and the SZ centroid is of the order of the arcminute, well below the maximum radius considered in the WL analysis. The displacement is also very small with respect to r_{200}. Most of the times, the inner cut encompasses the shift. This makes the estimate of the total SNR within $3\,\mathrm{Mpc}\,h^{-1}$ mostly insensitive to the accurate determination of the centre (see Table 8).
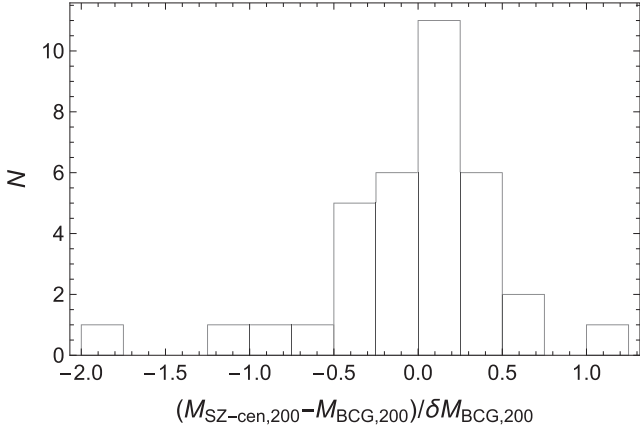
Figure 20. Distribution of the differences between masses measured around the BCG, $M_{\rm BCG,\,200}$, or around the SZ centroid, $M_{\rm SZ\text{-}cen,\,200}$. Differences are in units of the statistical uncertainties on $M_{\rm BCG,\,200}$.

Table 8. Masses and SNR determined assuming different centres, i.e. either the BCG or the SZ centroid. Column 1: cluster PSZ2 index. Columns 2, 3 and 4: displacement between the BCG and the SZ centroid in units of arcminutes, kpc h^{-1}, and r_{200}, respectively. Columns 5 and 6: mass and SNR assuming that haloes are centred in the BCG. Columns 7 and 8: same as columns 5 and 6 but assuming the SZ centroid as centre. Masses are in units of $10^{14}\,{\rm M}_\odot\,h^{-1}$.

|	$\Delta_{\rm BCG}$			BCG		SZ	
Index	(arcmin)	(kpc/h)	(r_{200})	M_{200}	SNR	M_{200}	SNR
21	1.42	88	0.06	7.0 ± 3.3	2.7	7.3 ± 4.0	2.7
38	2.20	80	0.12	0.8 ± 0.6	-0.2	0.7 ± 0.6	-0.4
43	0.30	9	0.01	2.9 ± 1.5	2.3	2.9 ± 1.6	2.2
212	0.30	59	0.03	16.5 ± 5.5	5.7	15.2 ± 4.3	5.7
215	0.62	69	0.09	1.2 ± 1.1	-0.3	0.8 ± 0.7	-0.2
216	1.02	160	0.19	1.7 ± 1.7	0.1	2.1 ± 1.8	-0.2
243	0.88	198	0.29	1.2 ± 1.2	0.1	1.7 ± 1.6	-0.1
251	1.81	272	0.22	5.7 ± 2.0	1.9	1.6 ± 1.5	0.8
268	0.78	51	0.05	2.4 ± 1.6	1.8	2.2 ± 1.4	1.8
271	1.68	339	0.34	3.4 ± 2.2	1.7	1.4 ± 1.6	1.0
329	0.80	132	0.08	12.1 ± 7.3	3.0	15.1 ± 7.4	2.9
360	1.41	250	0.23	4.3 ± 2.9	1.2	3.0 ± 2.1	1.2
370	0.75	78	0.08	2.8 ± 2.8	1.4	3.3 ± 3.2	1.4
391	0.99	175	0.10	15.0 ± 5.5	5.3	13.8 ± 4.1	5.0
446	1.19	124	0.10	5.5 ± 1.8	4.5	5.3 ± 1.8	4.2
464	2.47	257	0.19	7.1 ± 1.9	5.5	5.8 ± 1.9	4.7
473	1.01	82	0.11	1.2 ± 0.7	2.3	1.3 ± 0.7	2.3
478	0.64	183	0.16	6.7 ± 3.6	2.9	7.9 ± 4.2	2.9
547	1.43	92	0.06	8.7 ± 4.9	2.9	10.3 ± 4.7	3.3
554	0.29	65	0.05	6.7 ± 5.6	2.4	7.8 ± 5.4	2.3
586	1.17	313	0.31	4.5 ± 3.4	0.5	1.0 ± 1.1	-0.3
618	1.63	60	0.04	12.1 ± 6.5	4.2	15.8 ± 7.1	4.3
721	1.43	377	0.38	4.1 ± 4.8	0.9	5.6 ± 4.5	1.3
724	0.22	22	0.01	14.6 ± 5.2	6.5	15.6 ± 5.6	6.4
729	0.47	65	0.08	1.5 ± 2.0	1.4	0.7 ± 0.9	1.4
735	0.70	173	0.20	2.5 ± 2.2	1.0	3.3 ± 2.5	1.3
804	1.35	140	0.16	1.7 ± 0.8	2.6	1.4 ± 0.7	2.2
822	1.41	184	0.17	3.4 ± 1.3	3.1	3.2 ± 1.5	2.9
902	0.52	108	0.09	6.7 ± 3.2	1.3	6.8 ± 3.2	1.2
955	0.47	105	0.11	3.4 ± 2.8	-0.1	3.7 ± 3.1	-0.3
956	1.11	147	0.10	7.9 ± 6.1	1.7	6.8 ± 4.0	1.8
961	1.21	341	0.42	2.6 ± 3.2	0.3	6.0 ± 5.6	0.2
1046	0.37	68	0.06	5.9 ± 2.0	2.2	6.2 ± 2.2	2.1
1057	1.63	219	0.16	6.9 ± 2.3	5.1	6.9 ± 3.9	4.3
1212	0.92	104	0.09	3.6 ± 3.1	0.9	4.2 ± 3.3	1.3
Stack	–	–	–	4.63 ± 0.47	14.3	4.61 ± 0.51	13.4
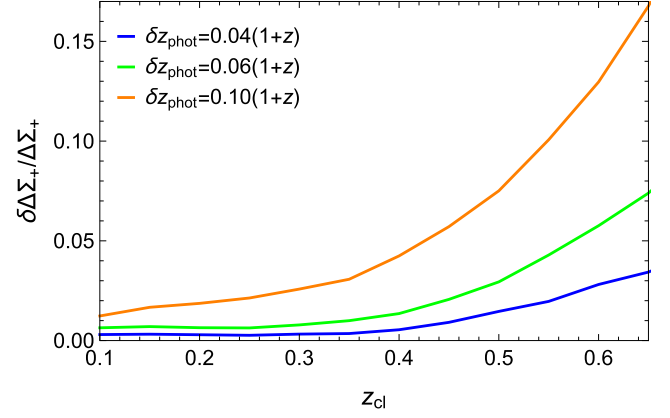
Figure 21. Systematic relative difference of lensing weighted differential density due to scatter in the photometric redshifts of the background galaxies.

13.6 Photometric redshift systematics

Photometric redshift systematics can impact WL analyses by biasing the estimation of the surface critical density $\Sigma_{\rm cr}$. For our estimator of the differential density, we computed the critical density for each source at the peak of the photometric redshift probability density. This is justified since we limited the selection of background galaxies to redshift ranges where the photo-z probability density distribution is mostly well behaved and single peaked (see Fig. 5).

Coupon et al. (2015) tested the impact of including high-redshift sources and the reliability of the point estimator for the critical density. They verified that photometric redshifts and shape measurements in CFHTLenS with additional NIR data are robust enough beyond $z_{\rm s} > 1.2$. They selected an arbitrary sample of low-redshift lens galaxies with a spectroscopic redshift and they measured the galaxy–galaxy lensing signal using all sources with $0.8 < z_{\rm s} < 1.2$ and all sources with $z_{\rm s} > 1.2$ and they found no significant difference between the two signals.

To quantitatively estimate the systematic error, we performed a simulation. We approximated the true redshift distribution of the field galaxies as the distribution of the measured photometric redshifts in a CFHTLenS field. The distribution of photometric redshifts was then simulated by considering a Gaussian error $\delta z_{\rm phot} \propto 1 + z_{\rm phot}$. We simulated the lens as a NFW toy model and extracted as background galaxies the sub-sample with $z_{\rm phot} > z_{\rm lens} + \Delta z_{\rm lens}$, with $\Delta z_{\rm lens} = 0.05$; see Section 5. We assigned to each source the true shear distortion and its real lensing weight from the shear catalog. We finally computed the $\Delta\Sigma_+$ estimator for the simulated input or the scattered redshifts. Results are summarized in Fig. 21 for different lens redshift and photo-z uncertainties.

For a redshift uncertainty of $\delta z_{\rm phot} \lesssim 0.06(1 + z_{\rm phot})$, as typical of the CHFTLenS survey in the range $0.2 \lesssim z_{\rm phot} \lesssim 1.2$ or for the RCSLenS in the range $0.4 \lesssim z_{\rm phot} \lesssim 1.2$, the systematic error on the differential density is below the percent level for lenses up to $z_{\rm cl} \sim 0.4$. For the highest redshift clusters in our sample at $z_{\rm cl} \gtrsim 0.6$, the uncertainty is ~ 5 per cent.

Together with the scatter, a bias in the estimated $z_{\rm phot}$ can affect the mass calibration. The bias, defined as the mean $(z_{\rm phot} - z_{\rm spes})/(1 + z_{\rm spec})$ including the outliers, in RCSLenS for sources with ODDS > 0.8 (as by our selection) is of the order of ~ 0.01 for redshifts in the range $0.4 \lesssim z_{\rm phot} \lesssim 1.0$, and it stays well below 5 per cent even relaxing the selection criteria (Hildebrandt et al. 2016).
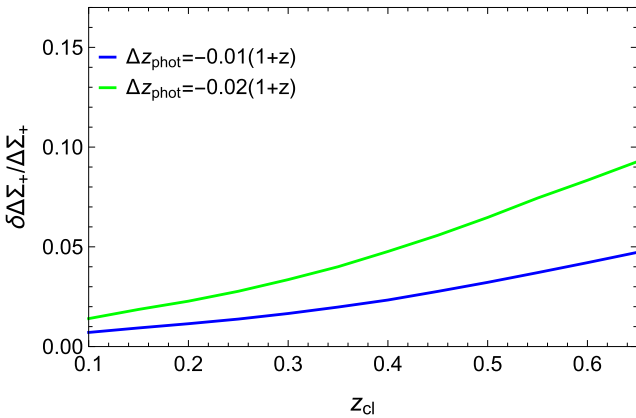
Figure 22. Systematic relative difference of lensing weighted differential density due to bias in the photometric redshifts of the background galaxies.

To quantitatively estimate the related systematic error in the mass calibration, we performed a simulation as before but we applied a constant bias rather than scattering the distribution of true redshifts. Results are summarized in Fig. 22. For a bias of -0.01, the systematic error on the shear signal is $\lesssim 2$ per cent in an ample lens redshift range.

Our treatment did not explicitly consider catastrophic outliers as a secondary population in the source redshift distribution. Outliers are defined as objects with $\Delta z = (z_{\mathrm{phot}} - z_{\mathrm{spes}})/(1 + z_{\mathrm{spec}})$ larger than an arbitrary threshold. In CFHTLenS, less than 4 per cent of estimated redshifts are regarded as outliers ($|\Delta z| > 0.15$; Hildebrandt et al. 2012). The fraction of outliers is significantly lower if galaxies are selected by the ODDS parameter (Hildebrandt et al. 2016).

However, we accounted for outliers in two ways, which can reproduce their main effects. First, the bias estimates include outliers. Secondly, we considered Gaussian distributions with quite extended tails. For $\delta z_{\mathrm{phot}}/(1 + z_{\mathrm{phot}}) = 0.1$ (0.06), ~ 13 (1.2) per cent of the sources are seen as outliers.

The systematic error on the mass, accounting for both scatter and bias, can be derived from the amplitude error of the lensing signal by using $\delta M_{200} \propto \Delta \Sigma_+^{0.65}$; see Appendix B. We can then estimate a mass uncertainty of ~ 5 per cent. Our result is in good agreement with the analysis in Melchior et al. (2017), who investigated how the estimate of the mean critical density varies as a function of lens redshift among different photometric redshift algorithms.

13.7 Shear systematics

A small calibration uncertainty in the shape measurements at the level of a few per cents can severely limit the accuracy on the mass (Umetsu et al. 2014; von der Linden et al. 2014a).

Multiplicative and additive biases in shape measurement for the CFHTLenS (Heymans et al. 2012; Miller et al. 2013) and the RCSLens (Hildebrandt et al. 2016) were identified on simulated images. The multiplicative bias mostly depends on the shape measurement technique rather than on the actual properties of the data and can be well assessed with a simulation-based estimate. The average calibration correction to the RCSLenS ellipticities is of the order of ~ 5 per cent (Hildebrandt et al. 2016).

Liu, Ortiz-Vazquez & Hill (2016) proposed a data-driven approach to calibrate the multiplicative bias m by cross-correlating CFHTLenS galaxy density maps with CFHTLenS shear maps and *Planck* CMB lensing maps. The additional correction for fainter

Table 9. Systematic error budget on the mass calibration of the PSZ2LenS clusters. Sources of systematics (column 1) are taken as uncorrelated.

Source	Mass error (per cent)
Shear measurements	5
Photometric redshifts	5
Line-of-sight projections	1
Contamination and membership dilution	3
Miscentering	0.5
Halo modelling	1
Total	8

galaxies may be relevant for cosmic shear analysis, but we could neglect it for our analysis.

Whereas simulation-testing shows that the multiplicative bias is well controlled, detailed comparison of separate shape catalogues of actual data can find that the residual systematic is larger. Jarvis et al. (2016) performed a detailed comparison of two independent shape catalogues from the Dark Energy Survey Science Verification data and found a systematic uncertainty of $\delta m \sim 0.03$. We can conservatively assume that this is the shear systematics affecting our analysis too, which entails a related mass uncertainty of ~ 4.5 per cent.

13.8 Line-of-sight projections

Two neighbouring clusters that fall along the line of sight may be blended by the SZ cluster finder into a single, apparently larger cluster. Whereas the Compton parameters add approximately linearly, projection effects can severely impact the WL mass. The lensing amplitude $\Delta \Sigma_+$ is a differential measurement and the estimated mass of the blended cluster can be well below the sum of the masses of the aligned haloes. Then, the blended object deviates from the mean scaling relation between SZ signal and mass.

To estimate this effect, we follow Simet et al. (2017). The systematic uncertainty due to projection effects can be approximated as

$$\delta M/M \sim \frac{p(\epsilon - 0.5)}{1 + p(\epsilon - 0.5)}, \tag{23}$$

where p is the fraction of aligned clusters and ϵ is an effective parameter which characterizes the effective mass contribution of the projected halo. The parameter ϵ depends on the relative position of the two blended haloes along the line of sight, and on their shape, elongation and concentration. If $\epsilon = 0.5$, we correctly estimate the total mass; if $\epsilon = 0$, the second halo is hidden and contributes no mass.

Planck objects are rare and the chance to have two or more of them aligned is small, $\lesssim 5$ per cent considering their tendency to be correlated. The systematic error on mass due to projection effects is then negligible ($\lesssim 1$ per cent).

13.9 Summary

Residual systematic and statistical uncertainties on the mass calibration not corrected for in our analysis are listed in Table 9. We assumed that systematics related to priors, mass estimators and radial range were properly accounted for and eliminated in our analysis. The main contributors to the systematic error budget are the calibration uncertainties of the multiplicative shear bias, the photo-z performance and the selection of the source galaxies. We

estimated that the total level of systematic uncertainty affecting our mass calibration and estimate of the *Planck* mass bias is ∼8 per cent.

Even though the systematics are specific to the data set and to the analysis, our systematic assessment is comparable to Melchior et al. (2017), who performed a WL mass calibration of redMaPPer galaxy clusters in Dark Energy Survey Science Verification data, and to Simet et al. (2017), who measured the WL mass-richness relation of the SDSS (Sloan Digital Sky Survey) redMaPPer clusters.

We did not consider as systematics triaxiality, orientation and substructures. The presence of substructures can dilute or enhance the tangential shear signal (Meneghetti et al. 2010; Becker & Kravtsov 2011; Giocoli et al. 2012, 2014), and lensing effects depend on the cluster orientation (Oguri et al. 2005; Sereno 2007; Sereno & Umetsu 2011; Limousin et al. 2013). For systems whose major axis points towards the observer, WL masses derived under the standard assumption of spherical symmetry are typically overestimated. The opposite occurs for clusters elongated in the plane of the sky, which are in the majority if the selected sample is randomly oriented.

We treated these effects as sources of intrinsic scatter, which quantifies the difference between the deprojected WL mass measurement and the true halo mass (Sereno & Ettori 2015b), rather than as systematic errors. In our regression scheme, we modelled the scatter of the WL mass, which we found to be 25 ± 18 per cent from the analysis of the mass–concentration relation (see Section 10) and 23 ± 15 per cent from the analysis of the *Planck* mass bias (see Section 12).

14 NOT CONFIRMED CLUSTERS

We could not confirm 7 out of the 47 candidate PSZ2 clusters in the CFHTLenS and RCSLenS fields. Out the subsample suitable for our WL analysis, i.e. the 41 candidate PSZ2 sources in the fields with photometric redshifts, we could not find evident counterparts for 6 candidates.

By visual inspection, we could detect neither any evident galaxy overdensity in the optical images nor an extended X-ray signal from archive *ROSAT* (Röntgensatellit) or *XMM*–Newton (X-ray Multi-Mirror) images near the candidates PSZ2 G006.84+50.69 (PSZ2 index: 25), G098.39+57.68 (463) and G233.46+25.46 (1062). We also did not find any galaxy cluster in the SIMBAD Astronomical Database within the uncertainty region associated with the PSZ2 source.

The analysis of the WL shear around them could not support the presence of a counterpart either. In particular, PSZ2 G006.84+50.69 (25) may be a substructure of the nearby larger PSZ2 G006.49+50.56 (21), i.e. Abell 2029. The SNR around the SZ centroid is 1.06 and the WL signal is compatible with no mass lens, $M_{200} = (0.4 \pm 0.4) \times 10^{14}\,\mathrm{M_\odot}\,h^{-1}$.

For PSZ2 G098.39+57.68 (463), we estimated an SNR = −0.83 by assuming as lens redshift the median redshift of the PSZ2 clusters, i.e $z = 0.224$.

The median redshift of the galaxies nearby PSZ2 G233.46+25.46 (1062) is $z_{\mathrm{phot}} = 0.85$. This supposed lens redshift is too high to perform a reliable WL analysis. We found just three source galaxies passing our criteria behind this candidate.

For two candidates, PSZ2 G084.69-58.60 (371) and G201.20-42.83 (912), a galaxy overdensity is seen in the photometric redshift distribution, but we could not assign a clear-cut BCG based on visual inspection or available information from the public catalogues. The WL signal around these candidates can be tentatively measured by locating the halo at the SZ centroid and estimating the redshift as

the peak of the distribution of measured z_{phot} along the line of sight. The SNR of PSZ2 G084.69-58.60 (371) and G201.20-42.83 (912) is 0.20 and −0.34, respectively. There is no indication from WL alone of the presence of a massive halo.

For two more candidate PSZ2 clusters, the identification was ambiguous because more than one counterpart could be assigned within the uncertainty region: PSZ2 G092.69+59.92 (421) and G317.52+59.94 (1496). For the source PSZ2 G092.69+59.92 (421), the closest candidate BCG, at $z_{\mathrm{spec}} = 0.59$, is located 3.8 arcmin away from the SZ centroid. The WL SNR around this position is 1.72, with a mass of $M_{200} = (3.2 \pm 2.8) \times 10^{14}\,\mathrm{M_\odot}\,h^{-1}$. For PSZ2 G317.52+59.94 (1496), there is a possible identification with a galaxy cluster at $z_{\mathrm{phot}} = 0.58$, but photometric redshifts for the background sources in the RCSLenS are not available in that regions, and so it is excluded from our final catalog.

15 CONCLUSIONS

Ongoing and future surveys are providing deep and accurate multiwavelength observations of the sky. SZ selected samples of clusters of galaxies have some very coveted qualities. In principle, they should provide unbiased and mass limited samples representative of the full population of cosmic haloes up to high redshifts.

To date, quality multiprobe coverage is still restricted to limited areas. We performed a WL analysis of the clusters of galaxies which were SZ selected by the *Planck* mission in the fields covered by the CFHTLenS and the RCSLenS. The surveys are not deep but the sample, which we named PSZ2LenS, is statistically complete and homogeneous in terms of observing facilities, and data acquisition, reduction and analysis.

Clusters are selected in SZ nearly independently of their dynamical and merging state. They should sample all kinds of clusters. In fact, we found that the *Planck* selected clusters are standard haloes in terms of their density profile, which is well fitted by cuspy halo models, and in terms of their concentrations, which nicely fit the ΛCDM prediction by numerical simulations. This suggests that the SZ detection does not suffer from overconcentration biases, as also inferred by Rossetti et al. (2017) based on the comparison of the X-ray properties of the highest SNR *Planck* clusters with X-ray selected samples.

Thanks to the statistical completeness of the PSZ2LenS sample, which is a faithful subsample of the whole population of *Planck* clusters, we could assess the bias of the SZ *Planck* masses by comparison with the WL masses. We found a mass bias of $-0.27 \pm 0.11(\mathrm{stat.}) \pm 0.08(\mathrm{sys.})$. We could estimate the effective bias over the full mass and redshift range of the *Planck* clusters. Most of the previous analyses considered small mass ranges, i.e. the massive end of the mass function, or they were limited to intermediate redshifts, where the WL signal is optimized. The most sensible comparison is with Sereno & Ettori (2017), who extended their analysis to lower masses and higher redshifts by exploiting a heterogeneous data set. Our results are in full agreement.

By comparison with WL masses, we confirmed that *Planck* masses are precise, i.e. the statistical uncertainties and the intrinsic scatter is small, but they are not accurate, i.e. they are systematically biased.

REFERENCES

Ahn C. P. et al., 2014, ApJS, 211, 17
Aihara H. et al., 2017, preprint (ArXiv:1702.08449)
Applegate D. E. et al., 2014, MNRAS, 439, 48
Arnaud M., Pratt G. W., Piffaretti R., Böhringer H., Croston J. H., Pointecouteau E., 2010, A&A, 517, A92
Auger M. W., Budzynski J. M., Belokurov V., Koposov S. E., McCarthy I. G., 2013, MNRAS, 436, 503
Bahé Y. M., McCarthy I. G., King L. J., 2012, MNRAS, 421, 1073
Baltz E. A., Marshall P., Oguri M., 2009, J. Cosmol. Astropart. Phys., 1, 15
Bartelmann M., Schneider P., 2001, Phisycs Rep., 340, 291
Battaglia N., Bond J. R., Pfrommer C., Sievers J. L., 2012, ApJ, 758, 74
Battaglia N. et al., 2016, J. Cosmol. Astropart. Phys., 8, 013
Becker M. R., Kravtsov A. V., 2011, ApJ, 740, 25
Beers T. C., Flynn K., Gebhardt K., 1990, AJ, 100, 32
Benjamin J. et al., 2013, MNRAS, 431, 1547
Bhattacharya S., Habib S., Heitmann K., Vikhlinin A., 2013, ApJ, 766, 32
Bielby R. et al., 2012, A&A, 545, A23
Bleem L. E. et al., 2015, ApJS, 216, 27
Bryan G. L., Norman M. L., 1998, ApJ, 495, 80
Bullock J. S., Kolatt T. S., Sigad Y., Somerville R. S., Kravtsov A. V., Klypin A. A., Primack J. R., Dekel A., 2001, MNRAS, 321, 559
Carrasco M. et al., 2017, ApJ, 834, 210
Cibirka N. et al., 2017, MNRAS, 468, 1092
Coil A. L. et al., 2011, ApJ, 741, 8
Coupon J. et al., 2015, MNRAS, 449, 1352
Covone G., Sereno M., Kilbinger M., Cardone V. F., 2014, ApJ, 784, L25
Cypriano E. S., Sodré L., Jr, Kneib J.-P., Campusano L. E., 2004, ApJ, 613, 95
Dahle H., 2006, ApJ, 653, 954
Dahle H., Kaiser N., Irgens R. J., Lilje P. B., Maddox S. J., 2002, ApJS, 139, 313
Diemer B., Kravtsov A. V., 2014, ApJ, 789, 1
Diemer B., Kravtsov A. V., 2015, ApJ, 799, 108
Du W., Fan Z., 2014, ApJ, 785, 57
Duffy A. R., Schaye J., Kay S. T., Dalla Vecchia C., 2008, MNRAS, 390, L64
Dutton A. A., Macciò A. V., 2014, MNRAS, 441, 3359
Eisenstein D. J., Hu W., 1999, ApJ, 511, 5
Erben T. et al., 2013, MNRAS, 433, 2545

Ettori S., Morandi A., Tozzi P., Balestra I., Borgani S., Rosati P., Lovisari L., Terenziani F., 2009, A&A, 501, 61
Formicola I., Radovich M., Meneghetti M., Mazzotta P., Grado A., Giocoli C., 2016, MNRAS, 458, 2776
Garilli B. et al., 2008, A&A, 486, 683
Garilli B. et al., 2014, A&A, 562, A23
George M. R. et al., 2012, ApJ, 757, 2
Gilbank D. G., Gladders M. D., Yee H. K. C., Hsieh B. C., 2011, AJ, 141, 94
Giocoli C., Tormen G., Sheth R. K., 2012, MNRAS, 422, 185
Giocoli C., Meneghetti M., Ettori S., Moscardini L., 2012, MNRAS, 426, 1558
Giocoli C., Meneghetti M., Metcalf R. B., Ettori S., Moscardini L., 2014, MNRAS, 440, 1899
Giodini S., Lovisari L., Pointecouteau E., Ettori S., Reiprich T. H., Hoekstra H., 2013, Space Sci. Rev., 177, 247
Gott, III J. R., Vogeley M. S., Podariu S., Ratra B., 2001, ApJ, 549, 1
Gruen D. et al., 2014, MNRAS, 442, 1507
Hamana T., Miyazaki S., Kashikawa N., Ellis R. S., Massey R. J., Refregier A., Taylor J. E., 2009, PASJ, 61, 833
Hasselfield M. et al., 2013, J. Cosmol. Astropart. Phys., 7, 008
Heymans C. et al., 2012, MNRAS, 427, 146
Hildebrandt H. et al., 2012, MNRAS, 421, 2355
Hildebrandt H. et al., 2016, MNRAS, 463, 635
Hoekstra H., 2003, MNRAS, 339, 1155
Hoekstra H., Donahue M., Conselice C. J., McNamara B. R., Voit G. M., 2011, ApJ, 726, 48
Hoekstra H., Mahdavi A., Babul A., Bildfell C., 2012, MNRAS, 427, 1298
Hoekstra H., Herbonnet R., Muzzin A., Babul A., Mahdavi A., Viola M., Cacciato M., 2015, MNRAS, 449, 685
Ilbert O. et al., 2006, A&A, 457, 841
Ilbert O. et al., 2009, ApJ, 690, 1236
Jarvis M. et al., 2016, MNRAS, 460, 2245
Johnston D. E. et al., 2007, preprint (arXiv:0709.1159)
Jullo E., Natarajan P., Kneib J.-P., D'Aloisio A., Limousin M., Richard J., Schimd C., 2010, Science, 329, 924
Kay S. T., Peel M. W., Short C. J., Thomas P. A., Young O. E., Battye R. A., Liddle A. R., Pearce F. R., 2012, MNRAS, 422, 1999
Kelly B. C., 2007, ApJ, 665, 1489
Kettula K. et al., 2015, MNRAS, 451, 1460
Klypin A. A., Trujillo-Gomez S., Primack J., 2011, ApJ, 740, 102
Klypin A., Yepes G., Gottlöber S., Prada F., Heß S., 2016, MNRAS, 457, 4340
Krause E., Pierpaoli E., Dolag K., Borgani S., 2012, MNRAS, 419, 1766
Laureijs R. et al., 2011, preprint (arXiv:1110.3193)
Lawrence A. et al., 2007, MNRAS, 379, 1599
Le Fèvre O. et al., 2005, A&A, 439, 845
Le Fèvre O. et al., 2015, A&A, 576, A79
Lieu M., Farr W. M., Betancourt M., Smith G. P., Sereno M., McCarthy I. G., 2017, MNRAS, 468, 4872
Limousin M., Morandi A., Sereno M., Meneghetti M., Ettori S., Bartelmann M., Verdugo T., 2013, Space Sci. Rev., 177, 155
Liu J., Ortiz-Vazquez A., Hill J. C., 2016, Phys. Rev. D, 93, 103508
Lubini M., Sereno M., Coles J., Jetzer P., Saha P., 2014, MNRAS, 437, 2461
Ludlow A. D., Navarro J. F., Angulo R. E., Boylan-Kolchin M., Springel V., Frenk C., White S. D. M., 2014, MNRAS, 441, 378
Ludlow A. D., Bose S., Angulo R. E., Wang L., Hellwing W. A., Navarro J. F., Cole S., Frenk C. S., 2016, MNRAS, 460, 1214
Mandelbaum R., Seljak U., Hirata C. M., 2008, JCAP, 8, 6
Mandelbaum R., Slosar A., Baldauf T., Seljak U., Hirata C. M., Nakajima R., Reyes R., Smith R. E., 2013, MNRAS, 432, 1544
Mantz A., Allen S. W., Rapetti D., Ebeling H., 2010, MNRAS, 406, 1759
Mantz A. B. et al., 2015, MNRAS, 446, 2205
Martin D. C. et al., 2005, ApJ, 619, L1
Medezinski E., Broadhurst T., Umetsu K., Oguri M., Rephaeli Y., Benítez N., 2010, MNRAS, 405, 257
Melchior P. et al., 2017, MNRAS, 469, 4899

Meneghetti M., Rasia E., 2013, preprint (arXiv:1303.6158)
Meneghetti M., Rasia E., Merten J., Bellagamba F., Ettori S., Mazzotta P., Dolag K., Marri S., 2010, A&A, 514, A93
Meneghetti M. et al., 2014, ApJ, 797, 34
Merten J. et al., 2015, ApJ, 806, 4
Miller L. et al., 2013, MNRAS, 429, 2858
Miyatake H. et al., 2015, ApJ, 806, 1
Motl P. M., Hallman E. J., Burns J. O., Norman M. L., 2005, ApJ, 623, L63
Navarro J. F., Frenk C. S., White S. D. M., 1997, ApJ, 490, 493
Oguri M., Hamana T., 2011, MNRAS, 414, 1851
Oguri M., Takada M., 2011, Phys. Rev. D, 83, 023008
Oguri M., Takada M., Umetsu K., Broadhurst T., 2005, ApJ, 632, 841
Oguri M., Bayliss M. B., Dahle H., Sharon K., Gladders M. D., Natarajan P., Hennawi J. F., Koester B. P., 2012, MNRAS, 420, 3213
Okabe N., Smith G. P., 2016, MNRAS, 461, 3794
Okabe N., Takada M., Umetsu K., Futamase T., Smith G. P., 2010, PASJ, 62, 811
Okabe N., Smith G. P., Umetsu K., Takada M., Futamase T., 2013, ApJ, 769, L35
Pedersen K., Dahle H., 2007, ApJ, 667, 26
Pierre M. et al., 2016, A&A, 592, A1
Planck Collaboration et al., 2014a, A&A, 571, A29
Planck Collaboration et al., 2014b, A&A, 571, A20
Planck Collaboration et al., 2016a, A&A, 594, A27
Planck Collaboration et al., 2016b, A&A, 594, A13
Planck Collaboration et al., 2016c, A&A, 594, A24
Prada F., Klypin A. A., Cuesta A. J., Betancort-Rijo J. E., Primack J., 2012, MNRAS, 423, 3018
Pratt G. W., Croston J. H., Arnaud M., Böhringer H., 2009, A&A, 498, 361
Rasia E. et al., 2012, N. J. Phys., 14, 055018
Rossetti M. et al., 2016, MNRAS, 457, 4515
Rossetti M., Gastaldello F., Eckert D., Della Torre M., Pantiri G., Cazzoletti P., Molendi S., 2017, MNRAS, 468, 1917
Schneider P., van Waerbeke L., Jain B., Kruse G., 1998, MNRAS, 296, 873
Sereno M., 2002, A&A, 393, 757
Sereno M., 2007, MNRAS, 380, 1207
Sereno M., 2015, MNRAS, 450, 3665
Sereno M., 2016, MNRAS, 455, 2149
Sereno M., Covone G., 2013, MNRAS, 434, 878
Sereno M., Ettori S., 2015a, MNRAS, 450, 3675
Sereno M., Ettori S., 2015b, MNRAS, 450, 3633
Sereno M., Ettori S., 2017, MNRAS, 468, 3322
Sereno M., Umetsu K., 2011, MNRAS, 416, 3187
Sereno M., Ettori S., Moscardini L., 2015, MNRAS, 450, 3649
Sereno M., Giocoli C., Ettori S., Moscardini L., 2015a, MNRAS, 449, 2024
Sereno M., Veropalumbo A., Marulli F., Covone G., Moscardini L., Cimatti A., 2015b, MNRAS, 449, 4147
Sereno M., Fedeli C., Moscardini L., 2016, J. Cosmol. Astropart. Phys., 1, 042
Shan H. et al., 2012, ApJ, 748, 56
Sheldon E. S. et al., 2004, AJ, 127, 2544
Sheth R. K., Tormen G., 1999, MNRAS, 308, 119
Shirasaki M., Nagai D., Lau E. T., 2016, MNRAS, 460, 3913
Simet M., McClintock T., Mandelbaum R., Rozo E., Rykoff E., Sheldon E., Wechsler R. H., 2017, MNRAS, 466, 3103
Smith R. E. et al., 2003, MNRAS, 341, 1311
Smith G. P. et al., 2016, MNRAS, 456, L74
Tanaka M. et al., 2017, preprint (arXiv:1704.05988)
Tinker J. L., Robertson B. E., Kravtsov A. V., Klypin A., Warren M. S., Yepes G., Gottlöber S., 2010, ApJ, 724, 878
Umetsu K. et al., 2014, ApJ, 795, 163
Umetsu K., Zitrin A., Gruen D., Merten J., Donahue M., Postman M., 2016, ApJ, 821, 116
Velander M. et al., 2014, MNRAS, 437, 2111
Viola M. et al., 2015, MNRAS, 452, 3529
Voit G. M., 2005, Rev. Mod. Phys., 77, 207
von der Linden A. et al., 2014a, MNRAS, 439, 2
von der Linden A. et al., 2014b, MNRAS, 443, 1973

Zhao D. H., Jing Y. P., Mo H. J., Börner G., 2009, ApJ, 707, 354
Zitrin A., Bartelmann M., Umetsu K., Oguri M., Broadhurst T., 2012, MNRAS, 426, 2944

APPENDIX A: RADIUS

Different recipes for the effective radius of a radial annulus have been proposed. A simple estimator is the mean of the inner R_{min} and outer R_{max} radii,

$$\langle R \rangle_{mean} = \frac{R_{min} + R_{max}}{2}. \tag{A1}$$

Alternatively, for a spatially uniform number density of background galaxies, the effective radius can be estimated as the area-weighted mean,

$$\langle R \rangle_{aw} = \frac{\int_{R_{min}}^{R_{max}} R^2 \mathrm{d}R}{\int_{R_{min}}^{R_{max}} R \mathrm{d}R} = \frac{2}{3} \frac{R_{min}^2 + R_{max}^2 + R_{min} R_{max}}{R_{min} + R_{max}}. \tag{A2}$$

The area-weighted mean is higher than the simple mean, since most of the area is near the outer radius.

Here, we define the effective radius $\langle R \rangle_{gw}$ as the shear-weighted radius,

$$g_+(\langle R \rangle_{gw}) = \frac{\int_{R_{min}}^{R_{max}} g_+(R) R \mathrm{d}R}{\int_{R_{min}}^{R_{max}} R \mathrm{d}R}. \tag{A3}$$

For a power-law shear profile, $g_+ \sim R^{-\alpha}$,

$$\langle R \rangle_{gw} = \left(\frac{2}{2-\alpha} \frac{R_{max}^{2-\alpha} - R_{min}^{2-\alpha}}{R_{max}^2 - R_{min}^2} \right)^{-1/\alpha}. \tag{A4}$$

Equations (A1) and (A2) are particular cases of equation (A4) for $\alpha = 1$ and -1, respectively.

In general, the logarithmic slope of the reduced shear profile, α, varies with the radius. The notable exception is the singular isothermal sphere with $\alpha_{SIS} = 1$. For most profiles the slope is close to one; see Fig. A1 for the case of the NFW halo.

In Fig. A2, we show that the simple mean, i.e. the shear-weighted radius with $\alpha = 1$, provides a very good approximation of the effective radius. The area-weighted radius, whereas the mean shear is underestimated, is larger than the effective radius. In fact, the area-weighting scheme accounts for most of the galaxies being near the upper radius but does not account for their lower shear.
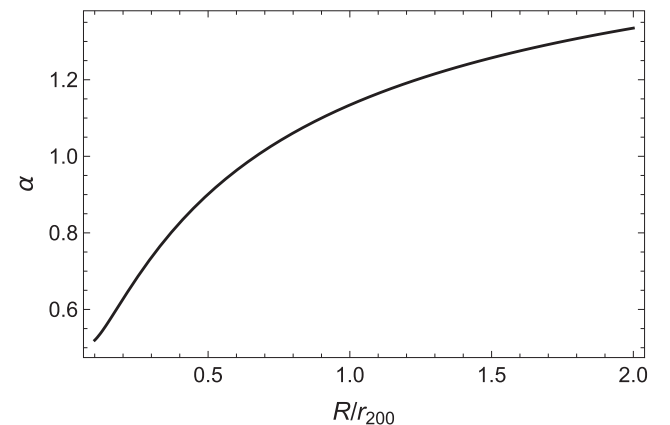

Figure A1. Logarithmic slope of the reduce shear profile as a function of radius for a NFW lens of mass $M_{200} = 5 \times 10^{14} \, M_\odot \, h^{-1}$ and concentration in agreement with the relation found in Dutton & Macciò (2014) for the *Planck* cosmology, i.e. $c_{200} \sim 3.78$. We placed the lens at $z_d = 0.5$ and the background sources at $z_s = 1.0$. The radius is in units of r_{200}.
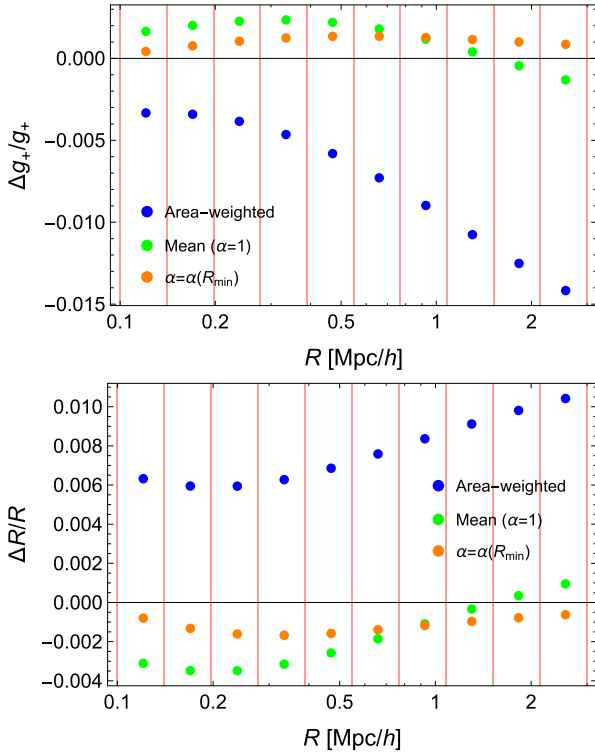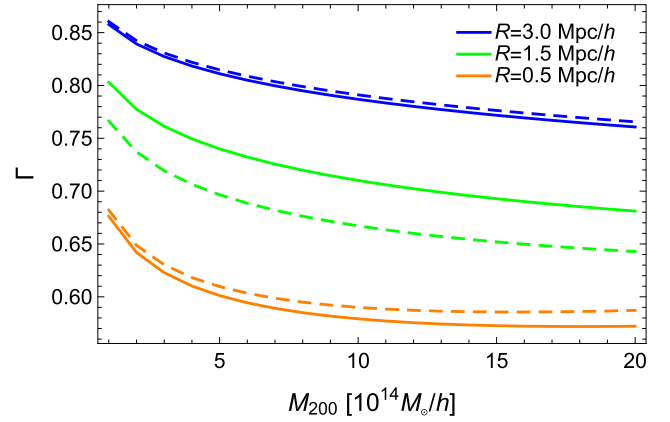
Figure B1. Logarithmic slope of the differential density profile of a NFW halo as a function of mass, $\Gamma = d\ln \Delta\Sigma_+ /d\ln M_{200}$ at different redshifts and radial distances from the cluster centre. Concentrations are assigned through the mass–concentration relation from Meneghetti et al. (2014). The full and dashed lines are for lenses at $z_{\rm cl} = 0.2$ and 0.4, respectively. The blue, green and orange lines (from top to bottom) are for radii $R = 0.5$, 1 and 3 Mpc h^{-1}, respectively.

Figure A2. Top panel: relative difference between the average reduced shear and the reduced shear computed at different radii. The vertical red lines delimit the radial annuli, which are 10 bins equally spaced in logarithmic units between 0.1 and 3 Mpc h^{-1}. The blue, green and orange points refer to effective radii computed as the mean, $\langle R \rangle_{\rm mean}$, the area-weighted mean $\langle R \rangle_{\rm aw}$ or the shear-weighted mean $\langle R \rangle_{\rm gw}$ with logarithmic slope computed at the inner radius. The lens properties are as in Fig. A1. Bottom panel: same as the top panel but for the relative difference between different estimators of the radius and the true shear-weighted radius.

Since the lens properties are not known when we stack the signal, the shear-weighted radius with $\alpha = 1$ is an acceptable choice. More elaborate schemes, as that fixing the slope at its value at the inner radius, which would nevertheless require some knowledge of the profile, do not improve the radius estimates significantly (see Fig. A2).

The previous discussion relied on the continuous limit where the background galaxy distribution is uniform and lies at a single redshift. For sparse populations which are redshift distributed, we have to compute the effective radius as

$$\langle R \rangle_{\rm gw} = \left(\frac{\sum_i w_i \Sigma_{{\rm cr},i}^{-2} R_i^{-\alpha}}{\sum_i w_i \Sigma_{{\rm cr},i}^{-2}} \right)^{-1/\alpha}, \tag{A5}$$

where we exploited the power-law approximation for the shear profile. The shear-weighted radius makes the fitting procedure to shear profiles less dependent on the binning scheme.

APPENDIX B: LENSING WEIGHTED AVERAGE

Stacking and combining lensing data or results is a highly nonlinear process. A sensible way to define the central estimate of a cluster property $\mathcal{O}$ for a lensing sample is the lensing weighted average (Umetsu et al. 2014),

$$\langle \mathcal{O} \rangle_{\rm lw} = \frac{\sum_i \mathcal{W}_i \mathcal{O}_i}{\sum_i \mathcal{W}_i}, \tag{B1}$$

where the sum runs over the cluster sample and the weight $\mathcal{W}$ of the i-th cluster is

$$\mathcal{W}_i = \sum_j w_{i,j} \Sigma_{{\rm cr},j}^{-2}, \tag{B2}$$

where the sum runs over the selected background galaxies behind the i-th cluster. The weight $\mathcal{W}$ accounts for the total shear weight of the cluster and accounts for the shear weight w of each lens-source pair, the lens and source redshifts through the critical density, and the angular size of the clusters, since lower redshift clusters subtend a larger angle in the sky for a fixed physical length and hence a larger number of background galaxies.

We verified, for example, that the definition in equation (B1) is appropriate to assign a redshift to the stacked profile, i.e. the recovered mass $M_{\rm stack}$ of a stacking sample of clusters with the same mass $M_{200} = M_{\rm cl}$ but at different redshifts is equal to $\langle M_{200} \rangle_{\rm lw} \simeq M_{\rm cl}$ if $z_{\rm stack} = \langle z_{\rm cl} \rangle_{\rm lw}$.

The lensing average in equation (B1) can be modified for some observables to account for the fact that we stack the density profiles $\Delta\Sigma_+$. In practice, we have to recover the mean observable from the stacked profile. If $\Delta\Sigma_+ \propto \mathcal{O}^\Gamma$, then (Melchior et al. 2017)

$$\langle \mathcal{O} \rangle_{\rm lw} = \left(\frac{\sum_i \mathcal{W}_i \mathcal{O}_i^\Gamma}{\sum_i \mathcal{W}_i} \right)^{1/\Gamma}. \tag{B3}$$

If we consider the mass as the observable, the exponent Γ can differ from 1. The dependence of the mass on the density profile can be approximated with a power-law $\Delta\Sigma_+ \propto M_{200}^\Gamma$ with

$$\Gamma = \frac{d\ln \Delta\Sigma_+}{d\ln M_{200}}; \tag{B4}$$

for an isothermal model, $\Gamma = 1$. For a NFW halo, the logarithmic density slope for a range of radii and redshifts is shown in Fig. B1. The slope is larger at small radii or large redshifts and spans a range from ~ 0.5 to 1. Based on some toy model simulations mimicking our stacking analysis, we found that $\Gamma \sim 0.65$ is appropriate for our range of masses and redshifts and for our fitting procedure.
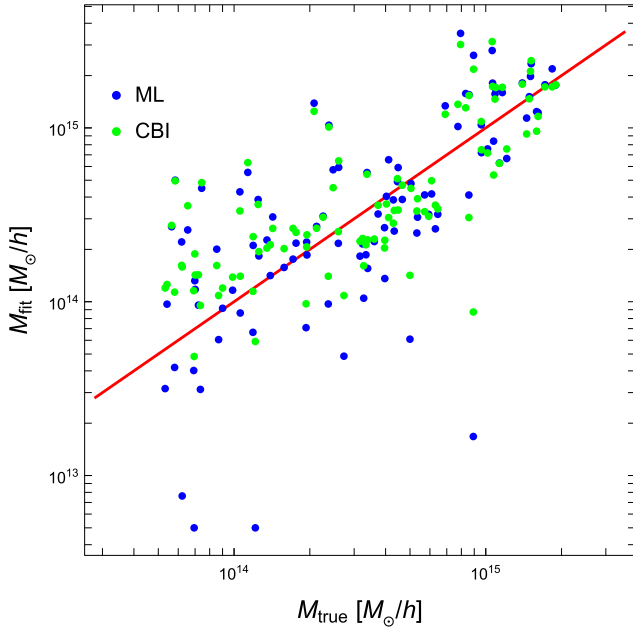
Figure C1. Fitted mass versus true input mass M_{200} for simulated NFW lenses. The green points and the associated error bars denote the central bi-weight estimator. The blue points denote the maximum likelihood estimator.

APPENDIX C: ROBUST ESTIMATOR

The posterior probability density function of the mass of low signal-to-noise ratio systems can be asymmetric or peaked near one of the imposed borders. As an extreme example, the more likely mass of a low mass group detected with a negative signal to noise ratio will coincide with the lower limit of the allowed parameter range. The problem is then to identify a reliable and stable mass estimator. The median (Gott et al. 2001) or the bi-weight location estimator C_{BI} (Beers et al. 1990) is regarded as robust choices for the central location and has been considered in WL analyses (Sereno & Umetsu 2011). Here, we want to compare the performances of the bi-weight location estimator against the maximum likelihood estimator.

We simulated the shear profile of clusters with shallow quality data. Lenses were modelled as NFW haloes at redshift $z_d = 0.3$. We assumed a shape noise error dominated by the intrinsic distribution of ellipticities, with a dispersion of $\sigma_e = 0.3$, and we also considered the noise from the large-scale structure. We considered a background population at $z_s = 0.8$ with a source density of $n_g = 2$ background galaxies per square arc minute.

We simulated 100 lens masses with a constant logarithmic spacing from $M_{200} = 5 \times 10^{13}$ to 2×10^{15} M$_\odot$ h^{-1}. Concentrations were associated assuming the scattered relation from Dutton & Macciò (2014). The shear profiles were finally simulated in 10 equally spaced logarithmic radial annuli between 0.1 and 3 Mpc h^{-1}.

We fitted the simulated profiles as in Section 8. Results are summarized in Fig. C1. At the high mass end ($M_{200} \gtrsim 10^{14}$ M$_\odot$ h^{-1}), the signal to noise is high enough and the estimated mass is stable whatever the estimator. At the low mass end, fluctuations are larger and differences can be significant. Results are usually consistent within the errors but the maximum likelihood estimator is more prone to outliers and often attracted towards the extremes of the allowed mass range. For our simulation, this problem is under control since we could fit the toy clusters with the right NFW profile. However, the problem can be exacerbated with real clusters which can deviate from the halo modelling we assume for the fit.

The bi-weight estimator is stabler but it can be influenced by the prior. Assuming a uniform prior, masses can be biased high at the low mass end. This would not be the case assuming a prior uniform in log space, which however could be inadequate at intermediate masses. Since most of the *Planck* clusters are expected to be $\gtrsim 10^{14}$ M$_\odot$ h^{-1}, the prior uniform in mass has to be preferred.

For the simulated lenses with $M_{200} > 10^{14}$ M$_\odot$ h^{-1}, the distribution of the relative deviations expressed as $\ln(M_{fit}/M_{true})$ has mean 0.03 (0.07) and standard deviation equal to 0.67 (0.91) for the bi-weight (maximum likelihood) estimator.

This paper has been typeset from a TEX/LATEX file prepared by the author.